

Thermal compensation system comissioning for O3 and
a study of the the Pockels effect of an AlGaAs coating

Syracuse University

Daniel Vander-Hyde

May 24, 2022

Abstract

Abstract goes here

Dedication

To my brother, Mikey.

Declaration

I declare that

Acknowledgements

Contents

1	Introduction	1
1.1	Gravitational wave detection	1
1.1.1	The Simple Michelson interferometer	2
1.1.2	Fabry-Perot Michelson (FPMI)	2
1.1.3	Dual-Recycled Fabry-Perot Michelson (DRFPMI)	3
1.2	aLIGO	5
1.2.1	Observing conditions	5
1.3	Noise	7
1.3.1	Brownian Thermal Noise	7
2	TCS comissioning for O3	13
2.1	aLIGO Thermal Compensation System (TCS)	13
2.2	Mode Matching in O3	14
2.2.1	Pre-loading for O3	14
2.3	Higher order TCS	19
2.3.1	Point absorbers	19
2.3.2	Actuation using a CO ₂ laser and mask	20
3	Electro-optic study of a GaAs/Al_{0.92}Ga_{0.08}As coated mirror	21
3.0.1	Anisotropic media	22
3.0.2	GaAs and Al _{0.92} Ga _{0.08} As crystal classification	26

CONTENTS

3.0.3	Induced anisotropy in zincblende crystals	27
3.0.4	Electro-optic modulation	29
3.0.5	Optical anisotropy of a HR GaAs / Al _{0.92} Ga _{0.08} As stack	30
3.0.6	Measured birefringence from HR GaAs/Al _{0.92} Ga _{0.08} As mirrors	34
3.1	Projected DARM coupling	34
3.2	Short, in-air, Pound-Drever-Hall locked, Fabry-Perot cavity experiment	35
3.2.1	PDH servo	36
3.2.2	Servo Parameters	40
3.2.3	Longitudinal Pockels Cell mirror mount assembly	43
3.3	Results	47
3.3.1	Measurement Calibration	48
3.3.2	Mounting Strategies	49
3.3.3	Drive coupling	53
4	Conclusion	55
5	Appendix	56
5.1	The Equipartition theorem and the Fluctuation dissipation theorem	56
5.2	AlGaAs coating orientation to beam polarization	58
5.3	Mode matching data for Electro-optic sample cavity	58
5.3.1	Pre MMT beam scan	58
5.3.2	“Just another mode matching tool” (JAMMT) solution	59
5.3.3	Post MMT beam scan	59
5.3.4	Laser PZT sweep	59
5.4	Calibration	59
5.5	Laplace calculator / code	60
5.6	MACOR assembly	61
5.7	HVA	62

CONTENTS

5.8 FSS	62
References	62

Chapter 1

Introduction

1.1 Gravitational wave detection

Mention initial detection summarize detections published from O1 to the end of O3.

1.1.1 The Simple Michelson interferometer

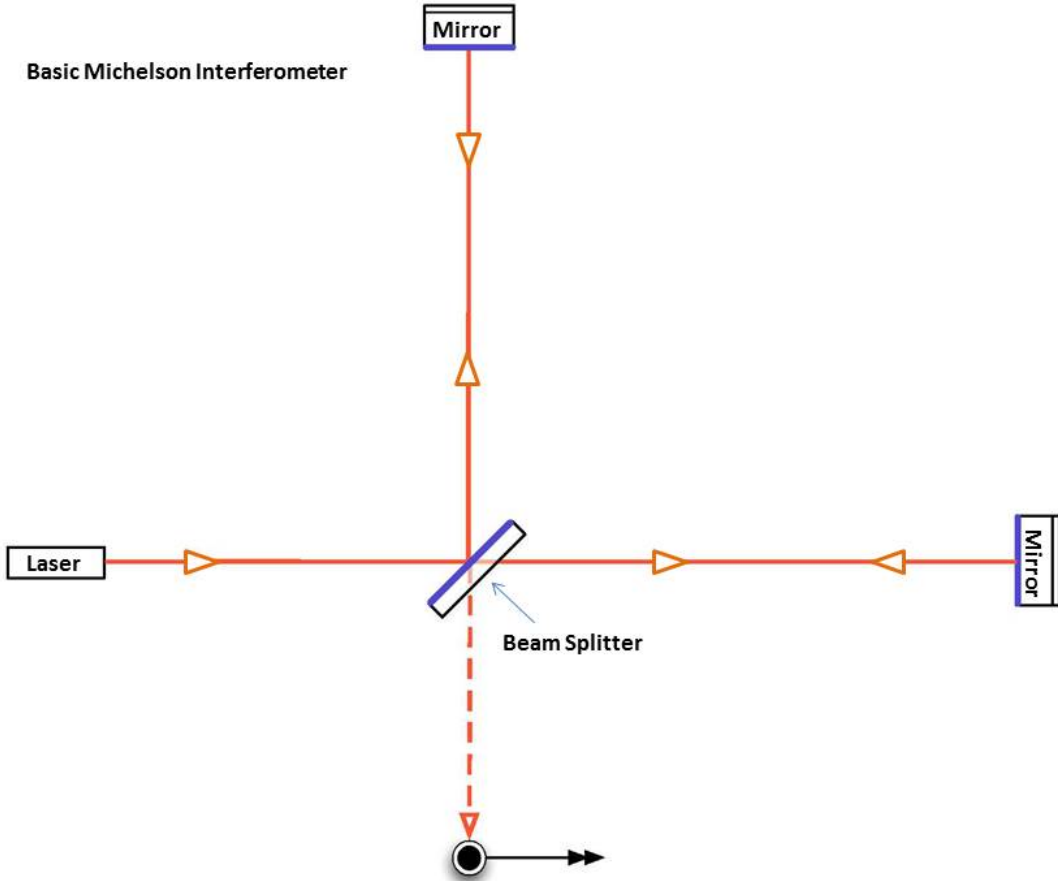


Figure 1.1: PENDING UPDATE The simple 4km Michelson with associated differential arm length response (left is optical schema, right is frequency response)

The frequency response of the Simple Michelson. Assuming a LIGO configuration (with 4km arm length), the differential arm response provides a reasonable optical gain until you reach a frequency that correlates to a gravitational wave period $\lambda/2$ to the interferometer arm length in such a way that the response is null.

1.1.2 Fabry-Perot Michelson (FPMI)

At the time of the proposal of LIGO, the creation of 4km long vacuum chambers was the most costly requirement for its construction [?]. When considering the possibility of constructing

gravitational wave detectors, two methods for arm extension were considered: the Delay Line and the Fabry-Perot cavity. The choice ultimately became the Fabry-Perot cavity.

The Fabry-Perot cavity

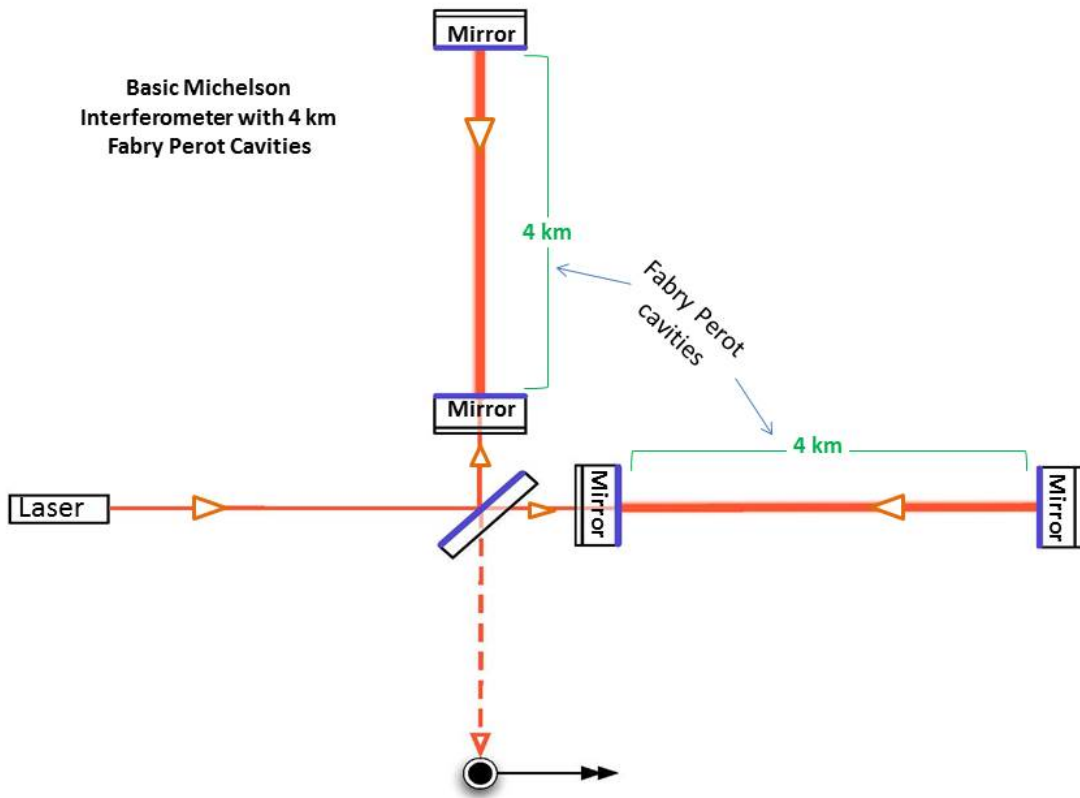


Figure 1.2: PENDING UPDATE The Fabry-Perot Michelson optical schema with associated differential arm length response (left is optical schema, right is frequency response)

1.1.3 Dual-Recycled Fabry-Perot Michelson (DRFPMI)

Recycling mirrors are an extension of the FPMI that provide a means of enhancing the optical gain of the instrument through different means by the nature of their placement at the symmetric and anti-symmetric ports.

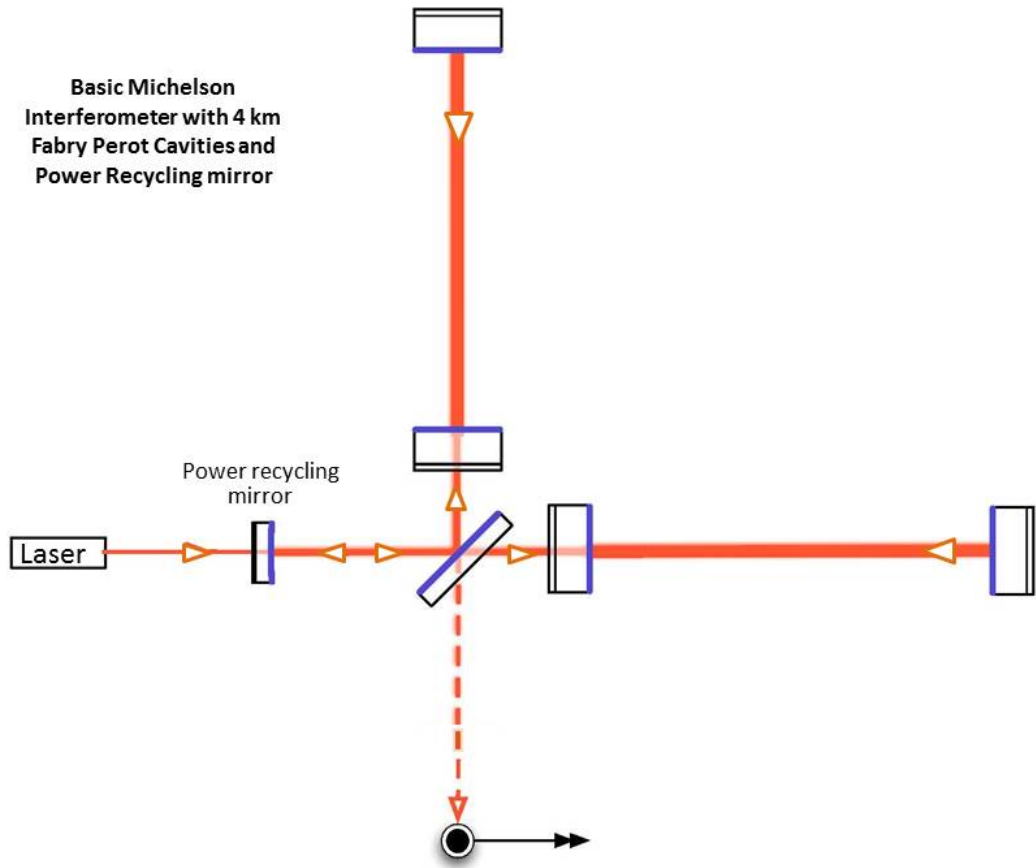


Figure 1.3: PENDING UPDATE (also, borrowed figure does not have SR mirror) The Dual-Recycled Fabry-Perot Michelson optical schema with associated differential arm length response (left is optical schema, right is frequency response)

Power Recycling

When operating a FPMI, power often gets reflected back to the symmetric port leading to a significant waste of power if simply dumped. An additional partially reflective mirror is placed at said port to recirculate (or “recycle”) that power back to the arm cavities. Its positioning is kept fixed enough so that the input light adds coherently with the laser input, while the macroscopic positioning from ITMX/Y is better understood once addressing resonance and optical sidebands.

Signal Recycling

This technique is commonly addressed to last because of it's contribution after considering the response from the PRFPMI. The principle can be understood similarly as most of the prior discussions; the use of a Fabry-Perot as an optical amplifier. By simply placing a mirror at the output port it is understood that you would take whatever light leakage coming from the PRFPMI (caused by differential arm motion) and re-introduce it to the arms. Now the question is, can that light add coherently for a signal that you are interested in detecting? As it turns out, it definitely can but careful choices must be made. Mirror location (macroscopic and microscopic tuning) as well as reflectivity have some interesting impacts to the cavity frequency response. But the general statement can be made: when introducing a mirror of relatively low reflectivity at the anti-symmetric port, you increase the detector bandwidth but at the cost of reducing the optical gain.

1.2 ALIGO

FIGURE: Of the ALIGO config “Core optics” (Recycling mirrors, Beam splitter, and FP cavity mirrors) are kept suspended with quadruple pendulum suspensions so to decouple seismic activity from the mirror positions.

1.2.1 Observing conditions

The requirements for the operation of the interferometer require that the interferometer be “Locked”; meaning that there are some necessary configurations / criteria in order for the instrument to act as an observatory with the designed sensitivity. Cavity length and alignment stabilization as well as mode matching are some general requirements for observatory operation.

Length Stabilization

With a coupled cavity configuration, maintaining mirror positions is imperative. Techniques such as the offset lock (using a DC photodiode to measure the transmitted, reflected, or circulating power within a linear and slightly off resonance point) [] and the Pound-Drever-Hall technique (reference section) are used to maintain cavity length stabilization.

FIGURE: ALS schema?

Gaussian Beams

So far, we've primarily discussed light and phase fronts in such a manner that hasn't addressed the important geometric constraint of using Gaussian laser light. We consider a general complex amplitude Gaussian beam propagating along the beam axis (z) with wavelength λ .

$$E(r) = E_o \frac{\sqrt{[\lambda z_o]/\pi}}{W(z)} e^{-r^2/W^2(z)} e^{-ikz - ik[r^2/(2R(z))] + i\zeta} \quad (1.1)$$

Where E_o is a complex amplitude, $r = \sqrt{x^2 + y^2}$ defines the transverse beam coordinates, k is the wave number, $W(z)$ is the beam width, $R(z)$ is the beam radius of curvature, and ζ is the Gouy phase.

Alignment Stabilization

Paraxial equation

HG modes

Mode Matching

LG modes

Optical Loss

Reduced power, Less effective squeezing

Mention thermal compensation system (TCS) but not too much detail

1.3 Noise

General noise budget (LHO and LLO O3?) or just GWINC?)

1.3.1 Brownian Thermal Noise

Might move this section back to the Al_{0.92}Ga_{0.08}As Electro-optic noise chapter

In 1827 the Scottish botanist Robert Brown noticed a constant motion of pollen particulates on the surface of water; witnessing randomized collisions of the water molecules holding a kinetic energy proportional to the temperature ($k_B T$) [1]. It is because of his documented observations we name the phenomena Brownian motion. And although the observations were on motion of particulates in liquids, molecules and atoms within gases and solids also exhibit Brownian motion. For high precision optical experiments operating at room temperature (and higher due to high power resonant beams), understanding how much differential phase noise is imparted on the interferometer light passing through and reflecting from core optics is crucial. This requires knowledge of the mean squared displacement from each degree of freedom of the system which can be realized through the Fluctuation Dissipation theorem. Derived by H.B. Callen and T.A. Welton, the theorem states that for a randomly fluctuating linear force [2]:

$$F_x^2(f) = 4k_B T \Re[Z] \quad (1.2)$$

Where $\Re[Z]$ is the real part of the impedance of the system. This impedance directly relates to equations of motion:

$$Z = \frac{F}{\dot{x}} \quad (1.3)$$

Another useful form is the power spectrum of the fluctuating motion:

$$x^2(f) = \frac{4k_B T}{(2\pi f)^2} \Re[Y] \quad (1.4)$$

Where Y is the inverse of the impedance or admittance. With this power spectra, modelling and budgeting notable LIGO fundamental noise contributions attributed to the choice of the materials used for mirror substrates, and highly reflective mirror coatings becomes less daunting. Though adequate modelling of internal force couplings for the aforementioned components is required.

Internal friction in Materials and Loss angle

Zener provides a model of the internal friction of materials incorporating anelasticity into the equations of motion [3]:

$$F = k(1 + i\phi)x + m\ddot{x} \quad (1.5)$$

Where m is mass attached to a spring with a spring constant $k(1 + i\phi)$ incorporating the degree of anelasticity ϕ . From equations 3.5 and 3.3 we perform a Laplace transform and acquire the following form of admittance:

$$Y(s) = \frac{\dot{x}(s)}{F(s)} = \frac{-s}{k(1 + i\phi) + ms^2} \quad (1.6)$$

Or more transparently the Fourier representation since we assume a linear time invariant system:

$$Y(\omega) = \frac{\dot{x}(\omega)}{F(\omega)} = \frac{-i\omega}{k(1 + i\phi) - m\omega^2} = \frac{k\omega\phi - i\omega(k - m\omega^2)}{(k - m\omega^2)^2 + k^2\phi^2} \quad (1.7)$$

Plugging equation 1.7 back into 1.4:

$$x^2(f) = \frac{2k_B T}{\pi} \frac{k\phi}{(k - 4\pi^2 m f^2)^2 + k^2 \phi^2} \quad (1.8)$$

Computing the admittance from a Gaussian beam impinging upon a HR mirror can require expansion of all individual mechanical degrees of freedom of the test mass system across a relevant frequency range, and with that approach convergence is not guaranteed. Saulson and Gonzalez provide an alternative method to computing the admittance coined the “direct approach” by Levin when computing the noise from a Gaussian beam on a LIGO HR test mass. The admittance can be acquired through:

$$\Re[Y] = \frac{W_{\text{diss}}}{F_o^2} \quad (1.9)$$

W_{diss} is the dissipated power from the system due to an oscillating force F_o . This form of the admittance reveals an important result of the fluctuation dissipation theorem where an undriven system with a dissipative actor, imparts motion to the degrees of freedom via a driving force by virtue of that same actor at finite temperatures. This direct approach also allows the surface pressure applied by the Gaussian beam to interrogate which mechanical modes of the test mass impose a significant energy when 1.9 is plugged into 1.4. In the case of the gaussian beam / uncoated test mass studied by Levin [4]:

$$S_x(f) = \frac{4k_B T}{f} \frac{1 - \sigma^2}{\pi^3 E_o r_o} I\phi \left[1 - O\left(\frac{r_o}{R}\right) \right] \quad (1.10)$$

Refer to Levin appendix for more on how elasticity parameters are introduced? Where ϕ and E_o are the Poisson ratio and Young’s modulus respectively, and $O(\frac{r_o}{R})$ contains a correction term contribution as a function of the small beam radius (r_o) relative to the mirror radius (R).

Coating Brownian thermal noise

Further investigations into the beam/optic system utilizing this approach and elasticity theory led to a deeper understanding about Brownian thermal noise contributions from LIGO test masses (substrate, suspensions, HR coating). Levin mentions, with details from Harry, that the noise contributed by a lossy mirror coating is proven to be the most significant contributor of brownian thermal noise. Hong provides a power spectral density [5]:

$$S_j^X = \frac{4k_B T \lambda \phi_x^j (1 - \sigma_j - 2\sigma_j^2)}{3\pi^2 f Y_j (1 - \sigma_j)^2 \omega_o^2} \quad (1.11)$$

Where X represents bulk and shear with j = odd (material 1) and j = even (material 2) alternating layers representing high and low index materials j = odd (material 1) j = even (material 2) for an HR coating.

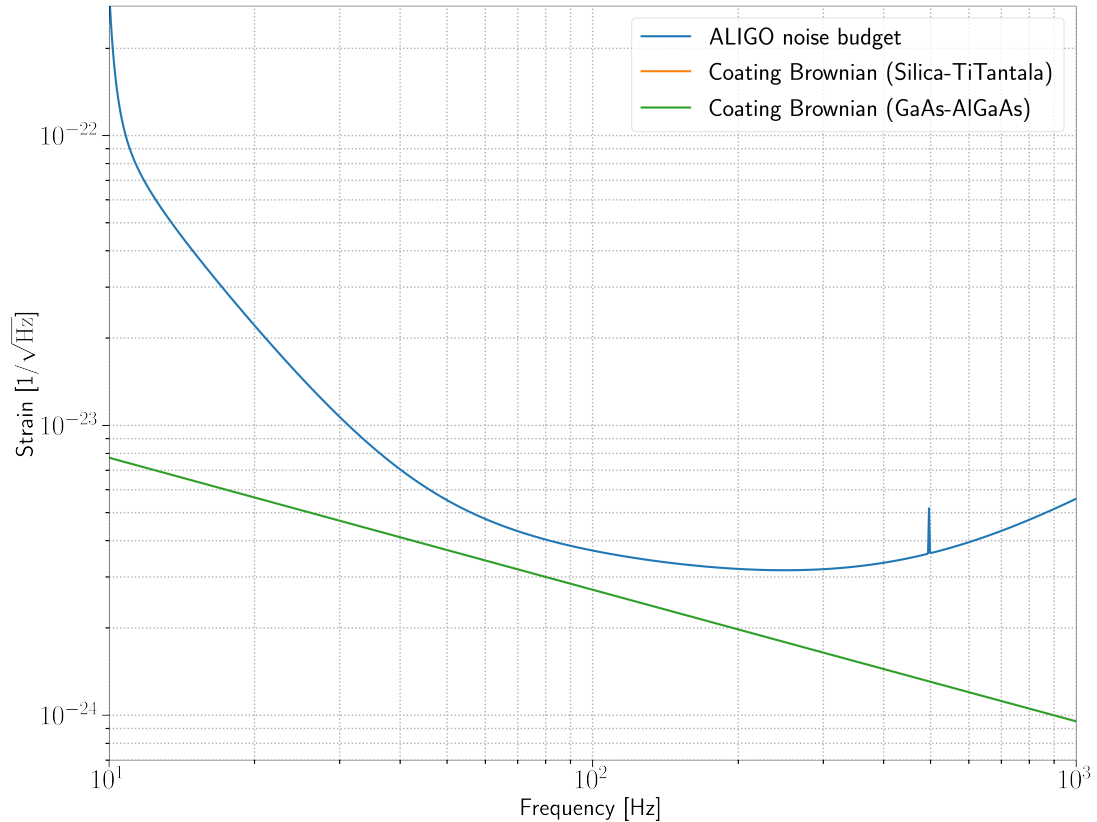


Figure 1.4: ALIGO noise budget placeholder for silica-tantala, and gaas-algaas brownian noise comparison

SiO₂/TiO₂ : Ta₂O₅ coating parameters

Currently the LIGO interferometers deposit $\lambda/4$ stacks of silica and titania doped tantalum on fused silica test mass substrates. Effective loss angle measurements [6]

Current SiO₂/TiO₂ : Ta₂O₅ elasticity params, power spectra, and strain spectral density (order of magnitude estimate)

GaAs/Al_{0.92}Ga_{0.08}As coating parameters

Specific coating parameters for most promising Al_{0.92}Ga_{0.08}As candidates? Chat with Steve.

Or just mention parameters that are listed in Cole 2013 [7]

Insert computed curves of the most precise and recent (effective) loss angle measurements (Nick Demos measurements?). More instructive to plot strain spectral density or displacement power spectra

Currently thermal noise from the SiO₂/TiO₂ : Ta₂O₅ optical coatings is the largest contributor of Brownian noise in LIGO compared to estimated substrate and suspension thermal noise [6]. As of the end of O3, Brownian thermal noise is estimated to be ? orders of magnitude below the current sensitivity and it will prove to be the limiting source of noise as that sensitivity is increased with various other upgrades mitigating fundamental and technical noise. (already mentioned in intro prior to this thermal noise section. Need to re-iterate in more detail?)

Chapter 2

TCS comissioning for O3

As shown in Chapter 1, increasing input power leads to a direct increase to the sensitivity of a DRFPMI to make gravitational wave detections. But one implication of this is the necessity for thermal compensation. As the interferometer increases input power, you directly couple more light into the Fabry-Pérot cavity arms; and even with optics ultra-low absorption ($\approx 400 \text{ ppb} \pm 150 \text{ ppb}$ [alog ? or point absorber paper](#)) still induce thermo-optic effects with the projected circulating arm power of 200 kW. A symptom of this is mode mismatch throughout the interferometer, a problem that contributes to loss of usable optical power throughought the DRFPMI which can reduce sensitivity two-fold: loss of power to your readout, and reduced efficacy of the current solution to reduce the quantum noise limit (squeezing).

2.1 aLIGO Thermal Compensation System (TCS)

Thermal deformations of mirrors can be superimposed, allowing an approximate restoration of the desired mirror radius of curvature with the usage of thermal actuators on the Fabry-Perot cavity mirrors at high power

- Annular actuation with RH actuators (Some notes about the analytical calculations of

RH (There is a paper on this).

- Central heating with central CO₂ laser

Wavefront sensing

Hartmann Wavefront Sensors

2.2 Mode Matching in O3

Countering the problems that occur at high circulating power requires estimated pre-load settings at higher power with the assumption that the test masses act as uniform absorbers. The presence of high absorption points on the test masses (aka point absorbers) required adjustments to the TCS pre-load and various ring heater and CO₂ settings were sampled. Part of this sampling lead to the development of a input ring heater filter allowing actuation to reach ? percent of the desired optical power within 2 hours compared to the 12 hour response pre-filter. Higher spatial frequency actuation in the form of a CO₂ mask was also tried.

2.2.1 Pre-loading for O3

Reference to TVO's thesis for pre-loading settings based on his model [8]

Optimizing RH thermo-optic response

With the inherent

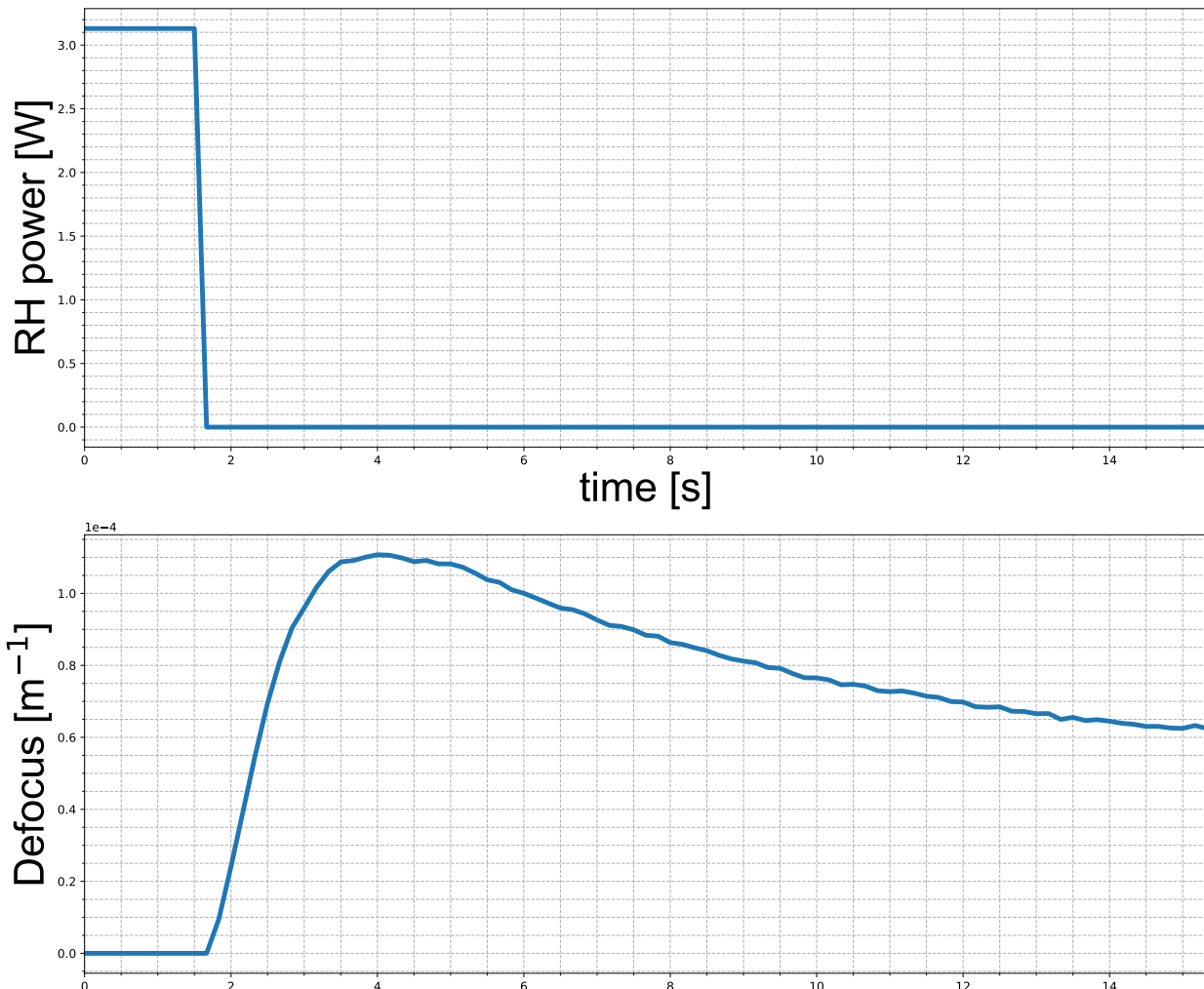


Figure 2.1: ITMY thermo-optic response to a 3.13 Watt power reduction to ring heaters. It's after ≈ 12 hours after the change was made do you start to see a small enough $\frac{d\alpha_{sp}}{dt}$ when you can assume a steady thermal lens.

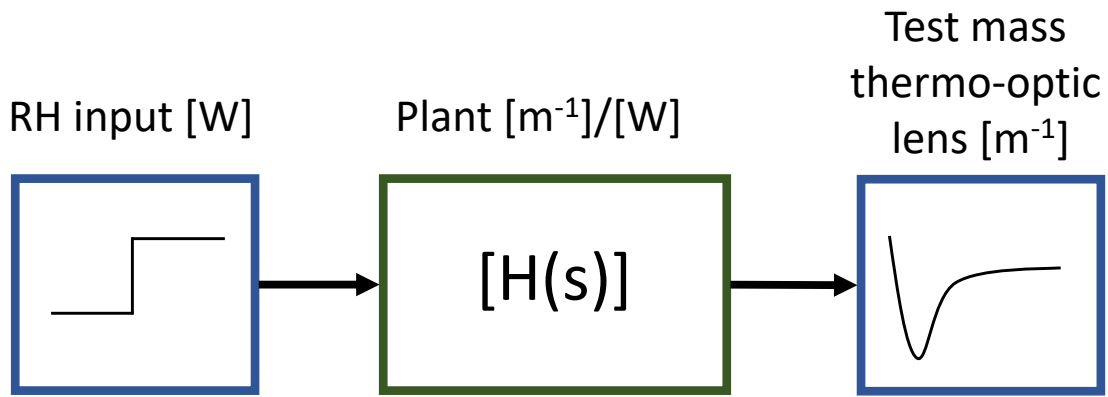


Figure 2.2: A pictograph showing how the plant transforms the signal. The example of this can be seen in Fig [2.1]

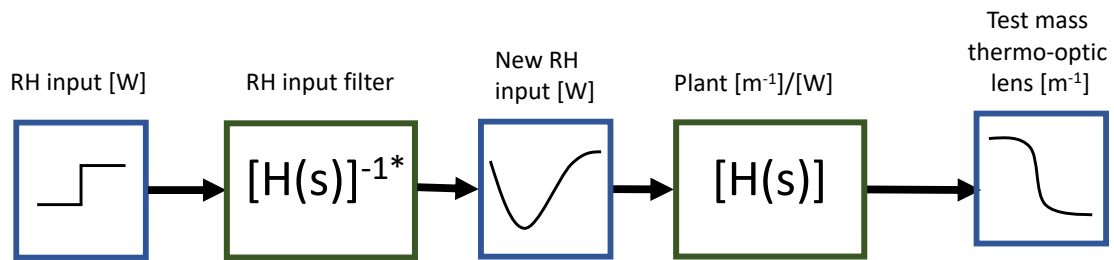


Figure 2.3: A pictograph showing the system with real time digital filtering for an improved thermo-optic response. The RH input filter is created by inverting the plant filter combine with a low pass and added poles to the zpk model to ensure stability.

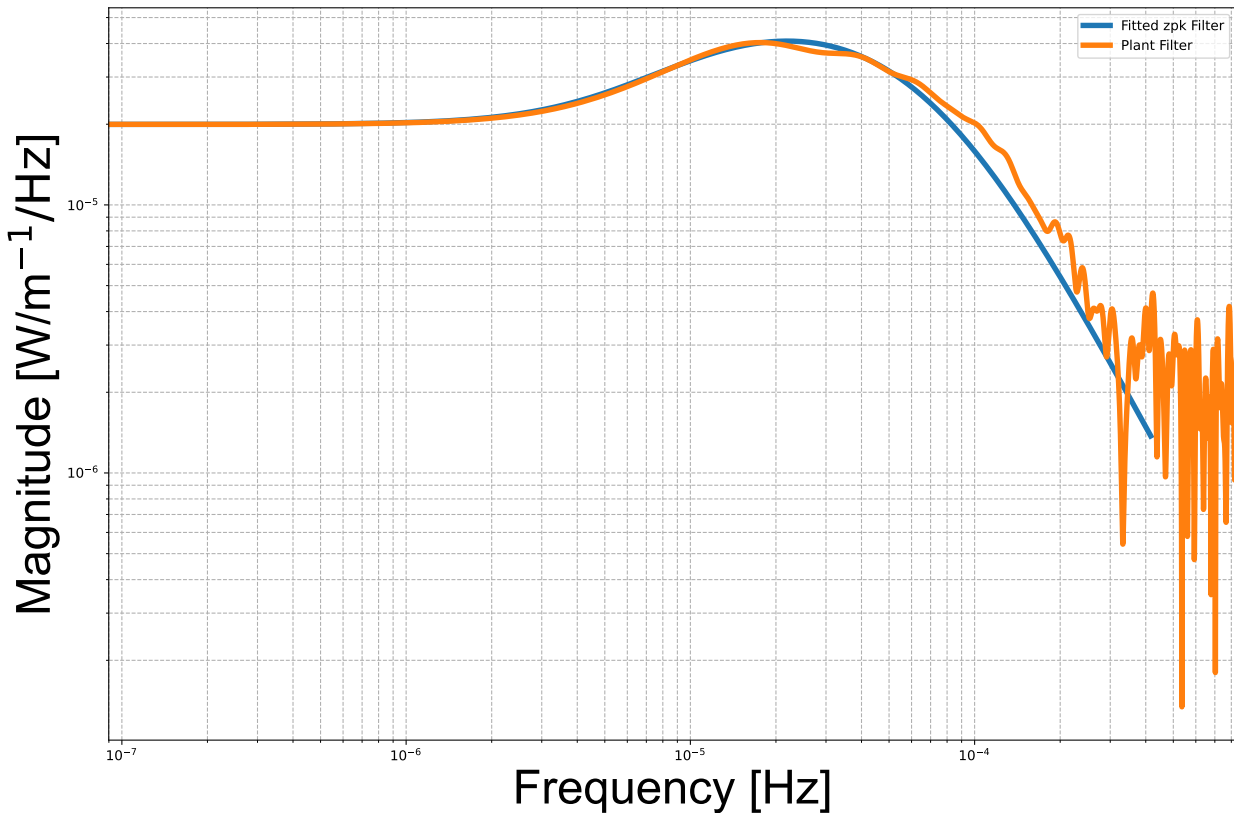


Figure 2.4: Showing the PSD of the RH response (normalized by the input RH power) over a an ≈ 12.5 hour period. The zpk model of the fitted filter ($H(s)$) is $9.2545e - 12 \frac{(s+3.14210e-5)}{(s+8.168e-5)(s+0.0003142)(s+0.0005969)}$

Dynamic Thermal compensation

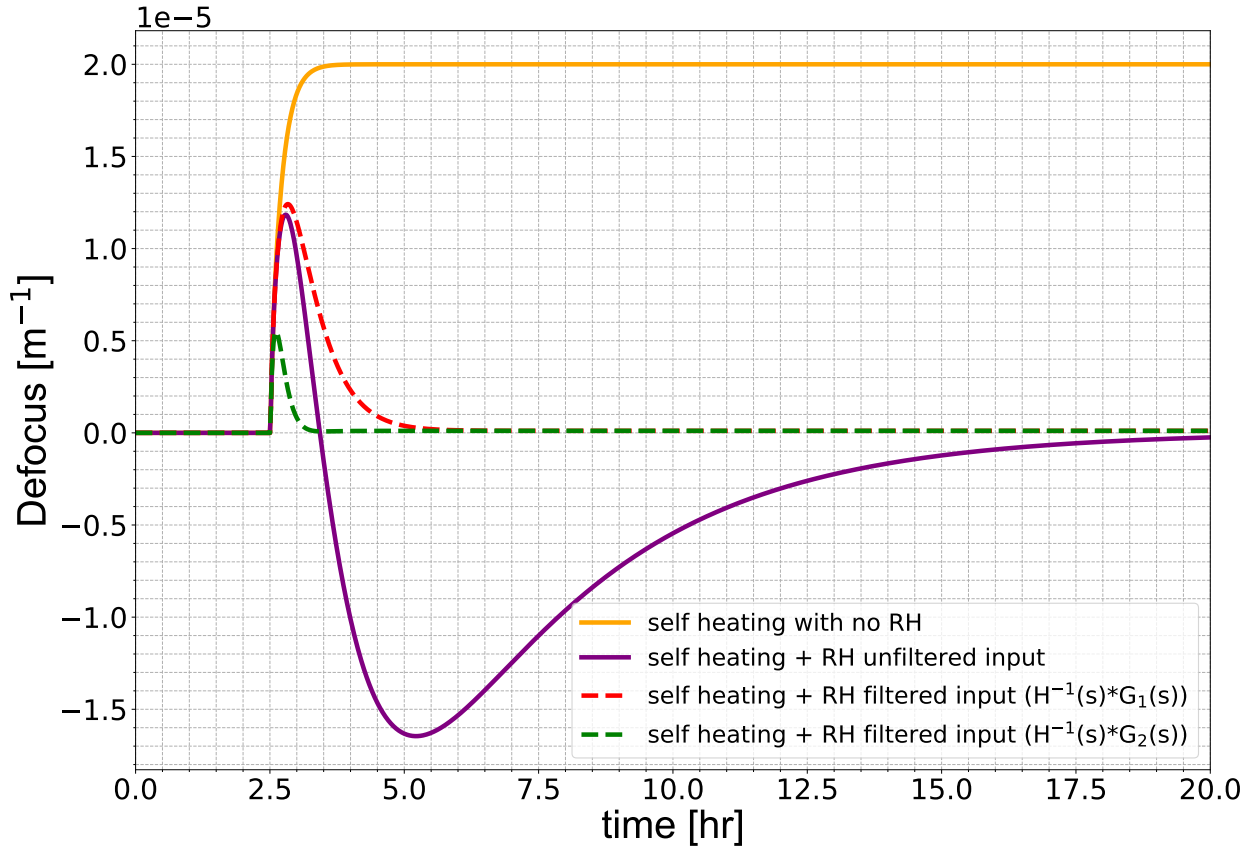


Figure 2.5: Comparison of the natural RH response and the response to the conditioned input. The above plot is simulated in Matlab by passing the RH input time series (top plot) through the $[H(s)]^{-1*}$ and $H(s)$ to acquire with the result lensing behavior on the bottom plot.

Limitations

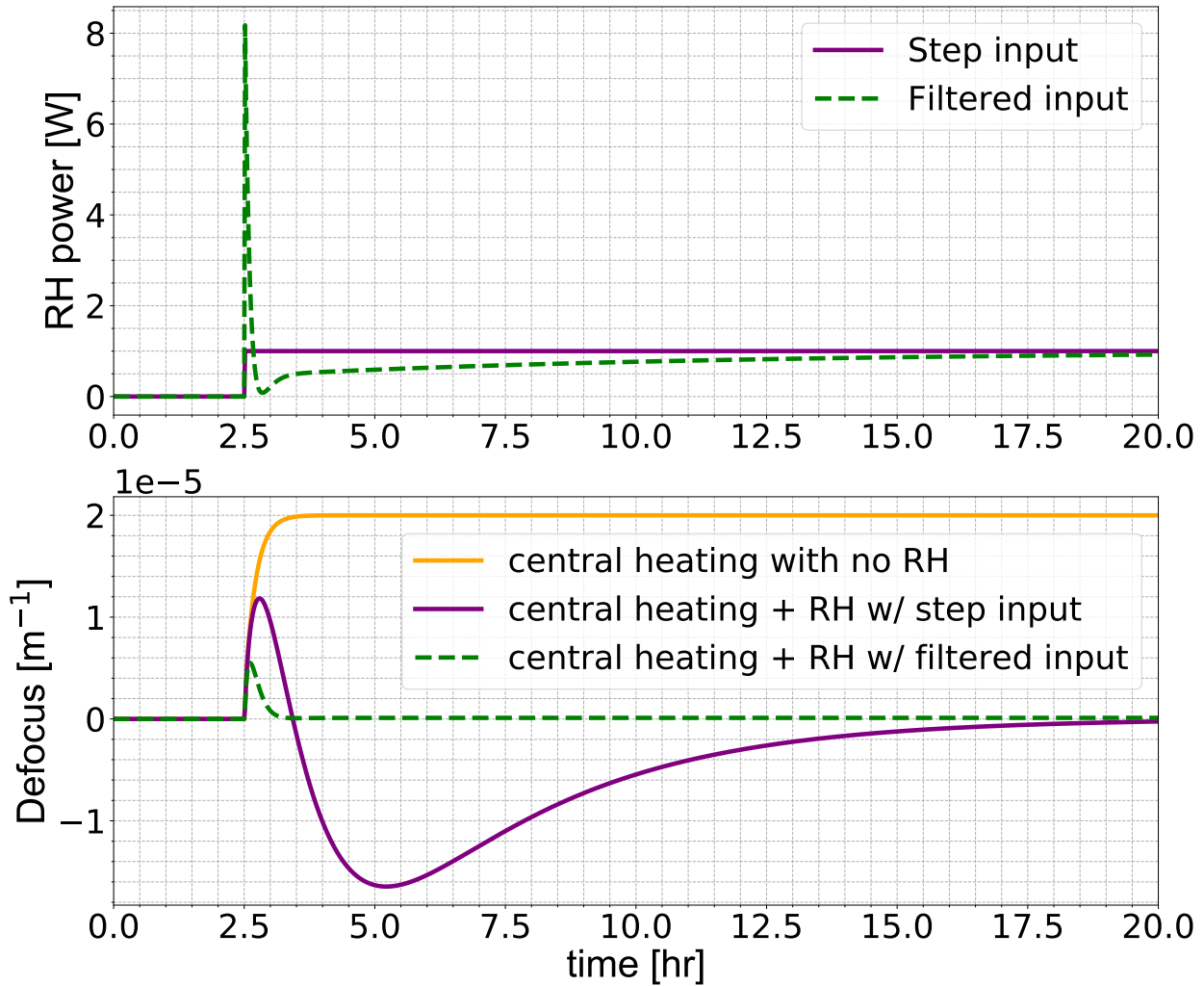


Figure 2.6: Comparison of the natural RH response and the response to the filtered input with RH power

Limitation on RH power is set at 8W **Double check source?**

Implementation into CDS at LHO (appendix?)

2.3 Higher order TCS

2.3.1 Point absorbers

- Impact on RF sidebands with interferometer thermalization

2.3.2 Actuation using a CO₂ laser and mask

- Aiden's design
- Imaging
- Installation
- Metric of improvement? (Impact on sidebands after thermalization) (Tracking dither line amplitudes)

Chapter 3

Electro-optic study of a GaAs/Al_{0.92}Ga_{0.08}As coated mirror

As mentioned in Section [?] one of the many LIGO fundamental noise sources is coating thermal noise from the SiO₂/TiO₂ : Ta₂O₅ aLIGO coatings. As aLIGO approaches its designed sensitivity various coating solutions are currently proposed to mitigate thermal noise coupling into the detector output [?]. With the potential to reduce coating Brownian noise by a factor of 10 [7], GaAs/Al_{0.92}Ga_{0.08}As shows much promise with next generation detectors for a potential strain reduction by a factor of 5 [?], in comparison to the current aLIGO coatings. Though inherent material property differences of these crystalline coatings introduce new and potentially significant noise couplings; one being the linear electro-optic property of crystalline materials (dn/dE), also known as the Pockels effect [9]. Prior to commitment of a GaAs/Al_{0.92}Ga_{0.08}As coating in gravitational wave detectors, a thorough study of these notable noises is worthwhile. This section details a study of starting with a survey of the distinguishing optical and material properties of crystalline materials like GaAs and Al_{0.92}Ga_{0.08}As by reviewing: light propagation through anisotropic materials, and induced optical anisotropy of zincblende materials. Immediately after, estimates of the differential phase of light reflected from a GaAs/Al_{0.92}Ga_{0.08}As coating caused by electric field

noise are computed with potential impacts to current generation gravitational wave detectors. With adequate motivation, an experiment designed to measure the pockels effect from a HR GaAs/Al_{0.92}Ga_{0.08}As coated “witness” sample was constructed and the design, results are discussed.

3.0.1 Anisotropic media

Unlike with isotropic media, we cannot assume that the index of refraction of anisotropic media is the same for all chosen wave vectors. This is a direct consequence of the birefringence of anisotropic media; characterized by the dielectric, permittivity, and polarization tensors.

The Dielectric tensor

Further elaborating on the nature of a generalized dielectric tensor for any wavevector is required to proceed:

$$D_i = \varepsilon_{ij} E_j \quad (3.1)$$

Where D is the displacement vector and E is the electric field vector and ε is the dielectric tensor. The displacement vector for isotropic media is retrieved when $i = j$ and $\varepsilon_i = \varepsilon$. To further understand the nature of the dielectric tensor we assert Poynting’s theorem providing an energy conservation requirement:

$$\nabla \cdot \vec{S} = \frac{dU}{dt} \quad (3.2)$$

Where $\vec{S} = \vec{E} \times \vec{H}$ is the poynting vector and $U = \frac{1}{8\pi}(\vec{E} \cdot \vec{D} + \vec{B} \cdot \vec{H})$ is the electromagnetic field density. The reader is left to perform the exercise and show that in order for 3.2 to hold true given 3.1

$$\varepsilon_{ij} = \varepsilon_{ji} \quad (3.3)$$

Demonstrating that the dielectric tensor is symmetric - exhibiting only six unique terms. Diagonalizing the tensor, the presence of two unique eigenvectors and eigenvalues indicates the existance of two eigenpolarizations with paired eigenindices.

Monochromatic plane wave propogation

Revisiting Maxwell's equations for simple monochromatic plane wave solution gives provides further direction on how crystalline media may effect incident light. Further elaborating, the following assumptions are made:

$$\vec{E} = E_o e^{(i\omega(\frac{n}{c}\vec{r}\cdot\vec{s}-t))} \quad (3.4)$$

Where n is the index of refraction, c is the speed of light, \vec{r} is the position vector and \vec{s} is the unit wave normal.

$$\nabla \times \vec{H} = \frac{\partial \vec{D}}{\partial t} \quad (3.5)$$

Where \vec{H} is the magnetic field assuming the permeability μ , and the generalized displacement vector \vec{D} and electric field vector \vec{E} .

$$\nabla \times \vec{E} = -\mu \vec{H} \quad (3.6)$$

Reducing to only the displacement and electric fields:

$$\vec{D} = \frac{n^2}{\mu} [\vec{E} - \vec{s}(\vec{s} \cdot \vec{E})] \quad (3.7)$$

Maxwell's equations show that the electric field is not necessarily parallel to the displacement field and in most materials with non-zero polarizability tensors and dielectric tensors, it is not. But as specified above, the displacement vector, Electric field and unit wave normal are co-planar while remaining orthogonal to \vec{H} . Assuming we are operating within a coordinate

system aligned with the principal dielectric axes, we substitute 3.1 into 3.7:

$$E_i = \frac{n^2 s_i (\vec{E} \cdot \vec{s})}{n^2 - \mu \varepsilon_i} \quad (3.8)$$

From here it can be shown that for a general plane wave there exist two unique refractive index solutions within the constructed dielectric. Though using this result to show this requires revisiting geometrical conditions that are best visualized using a method introduced in the next section. **For a more rigorous proof, see Appendix H in [10]**

Indicatrix

Acquiring solutions of the two indices along with the corresponding directions of propagation in the crystal for a general plane wave with unit wave vector \vec{s} can be done via a convenient geometrical construction. The construction begins by considering a constant electric energy density (U_e) surface in the \vec{D} space; an ellipsoid is formed:

$$\frac{D_x}{\varepsilon_x} + \frac{D_y}{\varepsilon_y} + \frac{D_z}{\varepsilon_z} = 2U_e \varepsilon_o \quad (3.9)$$

With redefined coordinates $(\vec{D}/\sqrt{2U_e \varepsilon_o}) \rightarrow \vec{r}$ and setting $\varepsilon_i = n_i^2$:

$$\frac{x^2}{n_x^2} + \frac{y^2}{n_y^2} + \frac{z^2}{n_z^2} = 1 \quad (3.10)$$

This equation for the ellipsoid is known as the indicatrix. Given the co-planar solution demonstrated in the last section, we can impose the normal of the plane $\vec{r} \cdot \vec{s} = 0$:

$$\vec{r} \cdot \vec{s} = x s_x + y s_y + z s_z = 0 \quad (3.11)$$

Equations 3.9 and 3.11 both contribute constraints to the method of finding extrema using Lagrange multipliers for the function:

$$r^2 = x^2 + y^2 + z^2 \quad (3.12)$$

The Lagrangian (\mathcal{L}) with the introduced multipliers (λ_1, λ_2) then becomes:

$$\mathcal{L}(\vec{r}, \vec{s}, \lambda_1, \lambda_2) = x^2 + y^2 + z^2 + \lambda_1(xs_x + ys_y + zs_z) + \lambda_2\left(\frac{x^2}{\varepsilon_x} + \frac{y^2}{\varepsilon_y} + \frac{z^2}{\varepsilon_z} - 1\right) \quad (3.13)$$

With the generated system of equations from the Lagrange multiplier method ($\partial F_i / \partial x_i = 0$, and $\partial F_j / \partial \lambda_j$) where index $i = x, y, z$ and $j = 1, 2$ we obtain a system of 3 equations:

$$i\left(1 - \frac{r^2}{\varepsilon_i}\right) + s_i\left(\frac{xs_x}{\varepsilon_x} + \frac{ys_y}{\varepsilon_y} + \frac{zs_z}{\varepsilon_z}\right) = 0 \quad (3.14)$$

The result is verified when substituting $r \rightarrow \frac{\vec{D}}{\sqrt{\vec{E} \cdot \vec{D} \varepsilon_o}}$ back which recovers 3.8.

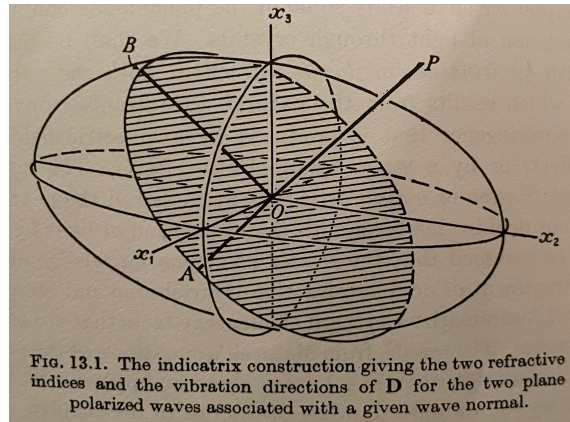


Figure 3.1: General ellipsoid indicatrix with a general propagation direction (Using Nye's figure as placeholder as of now)

3.0.2 GaAs and Al_{0.92}Ga_{0.08}As crystal classification

The space group of GaAs as well as Al_{0.92}Ga_{0.08}As are within the $F\bar{4}3m$ space group. Crystals of this particular space group are commonly known as zincblende crystals; a common crystal configuration named after zinc sulfide (ZnS). Cubic crystals by their crystallographic structure display optically isotropic characteristics when stress free and no DC and/or slowly varying electric fields are present. Is this true? Yes. Though the birefringence seen from HR GaAs coatings is said to be due to an “intrinsic stress” in the high and low index layers. (What is breaking the symmetry to cause this? Heteroepitaxy? Annealing? Defects? Is this birefringence the same for all samples?) I think a dedicated high precision birefringence measurement on multiple samples would be cool.

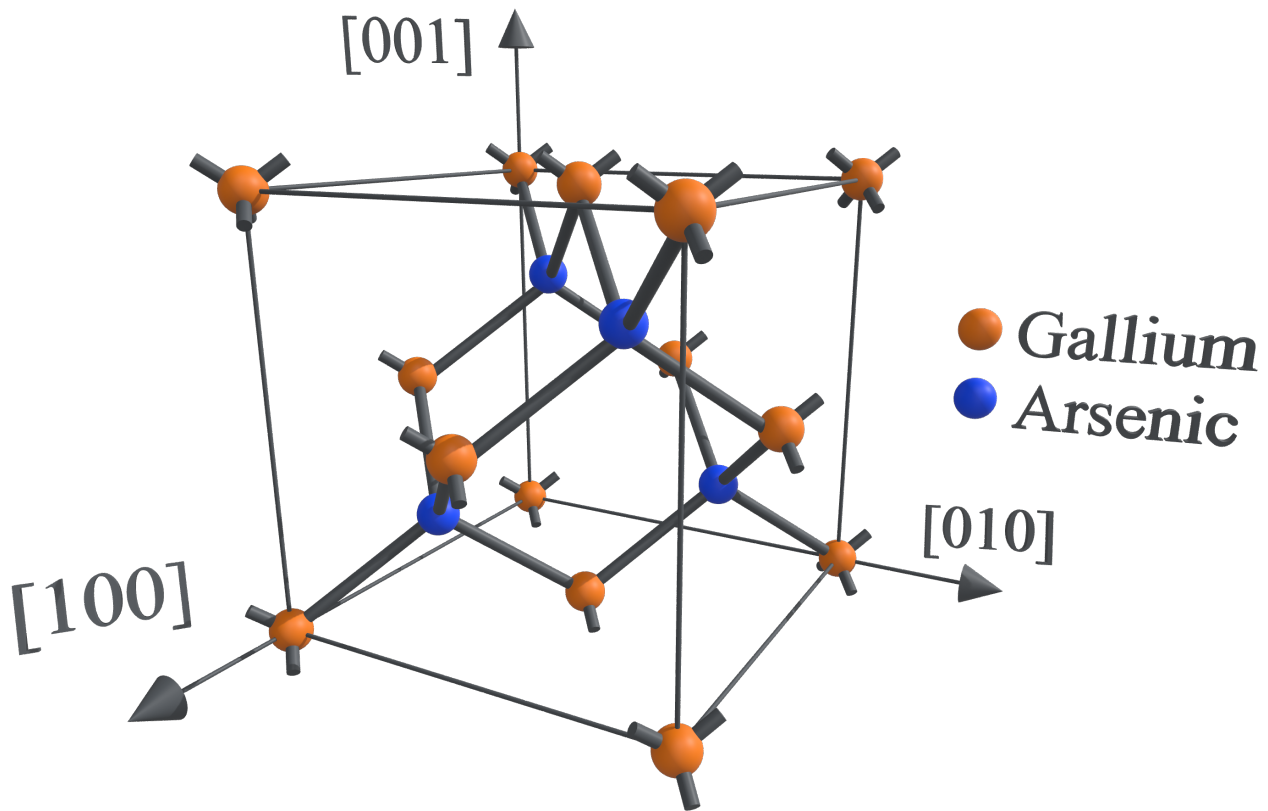


Figure 3.2: The unit cell of gallium arsenide (GaAs) with associated miller indices as coordinate axes

Mention the difference in lattice cell constant between GaAs and Al_{0.92}Ga_{0.08}As?

3.0.3 Induced anisotropy in zincblende crystals

Zincblende structures, like the crystalline materials in question can exhibit birefringent properties when under the influence of two factors: stress in the material, and present within DC electric fields. These two properties of crystalline materials are known as the photoelastic and electro-optic effects respectively.

The (linear) electro-optic (Pockel's) effect

For non-centrosymmetric crystalline media there exists a non-zero rank 2, 6×3 tensor (r_{ij}) connecting a low-frequency¹ electric field $\vec{E}(f) = [E_x(f), E_y(f), E_z(f)]$ directly to the indicatrix [11, 10]:

$$\begin{bmatrix} \left(\frac{1}{\Delta n^2}\right)_1 \\ \left(\frac{1}{\Delta n^2}\right)_2 \\ \left(\frac{1}{\Delta n^2}\right)_3 \\ \left(\frac{1}{\Delta n^2}\right)_4 \\ \left(\frac{1}{\Delta n^2}\right)_5 \\ \left(\frac{1}{\Delta n^2}\right)_6 \end{bmatrix} = \begin{bmatrix} r_{11} & r_{12} & r_{13} \\ r_{21} & r_{22} & r_{23} \\ r_{31} & r_{32} & r_{33} \\ r_{41} & r_{42} & r_{43} \\ r_{51} & r_{52} & r_{53} \\ r_{61} & r_{62} & r_{63} \end{bmatrix} \begin{bmatrix} E_x(f) \\ E_y(f) \\ E_z(f) \end{bmatrix} \quad (3.15)$$

The i index runs over the terms in the indicatrix equation:

$$\left(\frac{1}{\Delta n_x^2}\right)x^2 + \left(\frac{1}{\Delta n_y^2}\right)y^2 + \left(\frac{1}{\Delta n_z^2}\right)z^2 + 2\left(\frac{1}{\Delta n_{xz}}\right)xz + 2\left(\frac{1}{\Delta n_{yz}}\right)yz + 2\left(\frac{1}{\Delta n_{xy}}\right)xy = 1 \quad (3.16)$$

Detail on some prior knowledge of $f \leq f_{\max}$? (Pockels cell specs?)

¹"low frequency" meaning orders of magnitude smaller than an optical field it effects

r_{ij} for zincblende crystals ($r_{\bar{4}3m,ij}$)

The form of the electro-optic tensor for zincblende crystals (including GaAs and Al_{0.92}Ga_{0.08}As) reduces such that $r_{ij} = r_{41} = r_{52} = r_{62} \neq 0$ with all other terms being zero:

$$r_{\bar{4}3m,ij} = \begin{bmatrix} 0 & 0 & 0 \\ 0 & 0 & 0 \\ 0 & 0 & 0 \\ r_{41} & 0 & 0 \\ 0 & r_{52} & 0 \\ 0 & 0 & r_{63} \end{bmatrix} \quad (3.17)$$

Where also $r_{41} = r_{52} = r_{63}$

New principal (electro-optic) dielectric axis for zincblende structures

In general the principle dielectric axes of the new ellipsoid do **not** coincide with the axes of the ellipsoid of the unperturbed crystal. The form of the index ellipsoid for a zincblende crystalline material accounting for the electro-optic tensor and some generalized DC electric field \vec{E} expressed in terms of the crystallographic axes is given by:

$$\left(\frac{1}{n_o^2}\right)x^2 + \left(\frac{1}{n_o^2}\right)y^2 + \left(\frac{1}{n_o^2}\right)z^2 + 2r_{41}E_{[100]}yz + 2r_{41}E_{[010]}xz + 2r_{41}E_{[001]}xy = 1 \quad (3.18)$$

Where we have set $n_x = n_y = n_z = n_o$ for zincblende structures.

The two principal axes are given by the eigenvectors of the matrix given from the equation above:

$$\begin{bmatrix} \left(\frac{1}{n_o^2}\right) & r_{41}E_{[001]} & r_{41}E_{[010]} \\ r_{41}E_{[001]} & \left(\frac{1}{n_o^2}\right) & E_{[100]} \\ r_{41}E_{[010]} & r_{41}E_{[100]} & \left(\frac{1}{n_o^2}\right) \end{bmatrix} \quad (3.19)$$

The photoelastic effect

When a general strains $S_{kl}(r) = \frac{1}{2} \left[\frac{\partial u_k(r)}{\partial x_i} + \frac{\partial u_i(r)}{\partial x_k} \right]$ are applied to a material, the photoelastic tensor p_{idkl} relates to the indicatrix by the following relation:

$$\left(\frac{1}{\Delta n^2} \right)_{id} = p_{idkl} S_{kl} \quad (3.20)$$

Supplementary comment to the measured birefringence from the mentioned intrinsic strain of the high and low index layers

The generalized indicatrix

$$\left(\frac{1}{\Delta n^2} \right)_{ij} = r_{ij} E_j + p_{ijkl} S_{kl} \quad (3.21)$$

Need to fix these indices

New principal dielectric axes for zincblende structures (zincblende photoelastic tensor, zincblende electro-optic tensor)

3.0.4 Electro-optic modulation

A common application of this effect is phase modulation onto a optical carrier field. Electro-optic modulators or Pockel cells accomplish this by sandwiching two capacitor plates around crystal with a single electrical input port designed to take in a frequency (Ω) within a specified modulation bandwidth. When the field amplitude across the crystal is driven by a voltage controlled oscillation, we experience a change in the electro-optic tensor. The voltage amplitude of the signal input is proportional to the strength of the phase modulation on the optical carrier field of frequency (ω) and is commonly quantified in terms of a modulation index (β).

Consider specific crystal that gives us our $\beta \sin(\Omega t)$

$$E_{\text{inp}} = E_o e^{i\omega t + \beta \sin(\Omega t)} \quad (3.22)$$



Figure 3.3: PENDING UPDATES currently borrowed image from rp photonics Longitudinal and Transverse Pockels cells

This construction resembles that of the electrostatic optical mount used to drive a longitudinal electric field

3.0.5 Optical anisotropy of a HR GaAs / Al_{0.92}Ga_{0.08}As stack

Our interests primarily lie with the study of birefringent properties of a candidate highly reflective GaAs/Al_{0.92}Ga_{0.08}As mirrorstack. This section is intended to provide a comprehensive review by: 1) making considerations of crystal coordinates when asserting an optical axis on a highly reflective crystalline stack manufactured by Thorlabs, 2) citing coating parameters and observed intrinsic birefringence from the highly reflective coating stack in question, 3) analyzing differential linear electro-optic effect on the phase of a reflected beam, and 4) estimating the the differential phase noise in LIGO based on calibrated electric field measurements.

Miller indices for highly reflective coatings GaAs/Al_{0.92}Ga_{0.08}As coatings

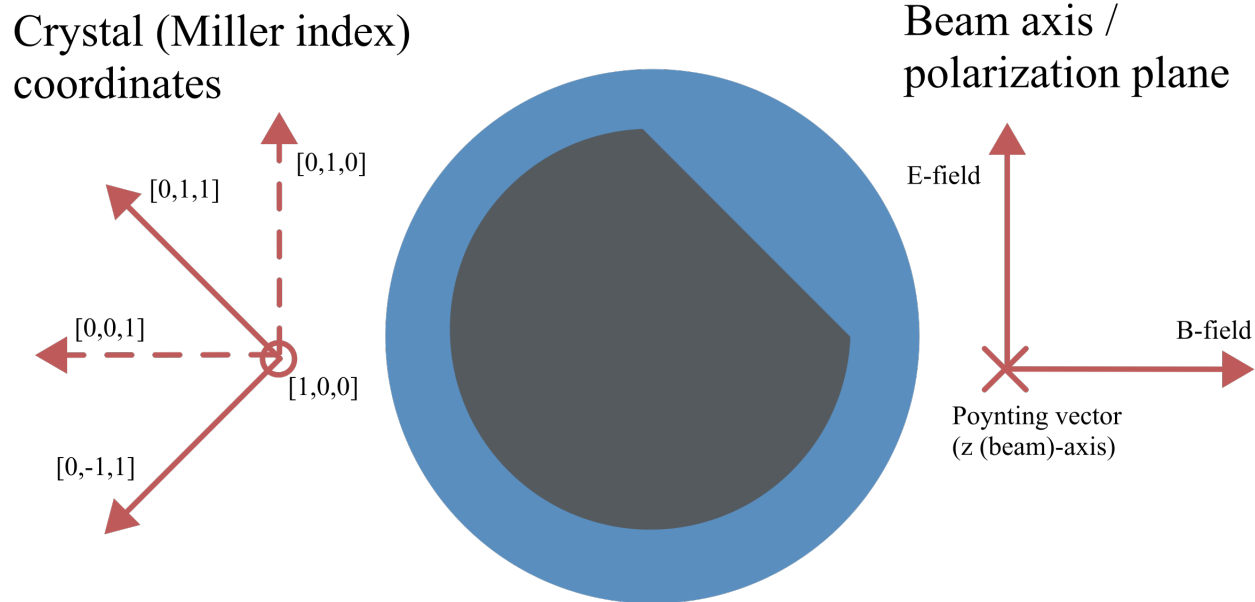


Figure 3.4: **PENDING UPDATES** Figure of the beam propagation axis with respect to the AlGaAs/GaAs crystal axes (not final version). Within the [100] plane the AlGaAs coating is grown with a flat indicator that draws a line within the [0-11] plane where the bisecting vector of the plane normal points towards the sample center. The axis formed by the [100] is parallel with the beam axis (z-axis). The polarizations of incident and reflected beam oscillate along vectors within the plane formed by the normal of that axis.

Up until this point we have discussed three different coordinate axes: the crystal axis (indicated by Miller index plane normals), the principal dielectric axis (coordinates based in diagonalization of the indicatrix), and an optical axis (when considering a desired (laser) light propagation). We assert the beam axis [?] with linearly p-polarized light.

Electro-optic coupling to the reflected phase of a HR mirror coating

With our coordinate considerations and established beam axis, it is now worth considering the influence of an isotropic white noise field ($E_n = [E_{nx}, E_{ny}, E_{nz}]$):

$$\begin{bmatrix} \left(\frac{1}{n_o^2}\right) & r_{41}E_{ny} & r_{41}E_{nx} \\ r_{41}E_{ny} & \left(\frac{1}{n_o^2}\right) & r_{41}E_{nz} \\ r_{41}E_{nx} & r_{41}E_{ny} & \left(\frac{1}{n_o^2}\right) \end{bmatrix} \quad (3.23)$$

Assuming E_n is small, the indicatrix change of E_{nx} and E_{ny} relative to E_{nz} (as seen by the beam polarization) will be small ($r_{41}E_{n(x/y)} \ll r_{41}E_{nz}$). After diagonalizing with relevant terms ² in the tensor, we are left with the following eigenindices:

$$\begin{aligned} n'_x &= n_o - r_{41}E_{nz} \\ n'_y &= n_o + r_{41}E_{nz} \end{aligned} \quad (3.24)$$

For GaAs @ 10.6 μ $r_{41} = 1.6 \times 10^{-12}$ [m/V]

Adachi estimate for Al_xGa_{1-x}As?

Relevant eigenpolarizations, non-optical field $E_y = E_z = 0$?

Figure: Transformed indicatrix (Before and after E_x)

Figure: Ellipse cross section. New eigenpolarizations and corresponding indices and their influence on incident field (Marty's result)

Assuming we are operating in a coordinate system suggested in Figure 3.4, which plane is impacted by some E_{noise} ? Revisiting the indicatrix we can see that for even non-zero z and y components that the only coupling to the input beam polarization is the index along the cross coupled zy axis through E_z is that of the E_x term. This gives us the ability to easily diagonalize the indicatrix tensor by setting the non-relevant field terms to zero. Fejer and Bonilla take an analytical approximation approach when finding the impact of the electric

²Note that the form of the tensor is still in the crystal coordinates but the E_n terms are placed in the tensor such that their directions align with beam axis coordinates.

field to the change in phase of the light through a crystalline anisotropic thin film ($\lambda/4$) stack [12].

$$\hat{\phi}' = \frac{\pi n_1 z}{1 - z^2} (z^{2N} - 1) \frac{z^{2N} \frac{(n_f)^2}{n_2 n_3} (n_2 \kappa_{\gamma 2} + n_3 \kappa_{\gamma 3}) - (n_2 \kappa_{\gamma 3} + n_3 \kappa_{\gamma 3})}{(n_1)^2 - (n_f)^2 z^{4N}} \quad (3.25)$$

with $z = \frac{n_2}{n_3}$ and $\kappa_{\gamma j} = \frac{d}{d\gamma} \log(n_j h_j)|_{\gamma=\gamma_O} \left(\frac{\hat{n}_j'}{\hat{n}_j} + \frac{\hat{h}_j'}{\hat{h}_j} \right)$

With κ being a scalar parameter.

FIGURE: Cross sectional view of multilayer coating

Numerical estimate

In the appendix of [13] Ballmer constructs a coating layer transfer function for a given coating layer k with index n_k , and thickness d_k , defining right and left propagating modes $\Psi^{R,L}$ respectively:

$$\begin{bmatrix} \Psi^R \\ \Psi^L \end{bmatrix}_{k+1} = Q_k D_k \begin{bmatrix} \Psi^R \\ \Psi^L \end{bmatrix} \quad (3.26)$$

D_k applies the phase ($\phi_k = 4\pi n_k d_k / \lambda_0$) from a given coating layer, and Q_k applies the transfer function between high-low/low-high index layers transition:

$$Q_k = \frac{1}{2n_{k+1}} \begin{bmatrix} n_{k+1} + n_k & n_{k+1} - n_k \\ n_{k+1} - n_k & n_{k+1} + n_k \end{bmatrix} \quad (3.27)$$

$$D_k = \begin{bmatrix} e^{-i\phi_k/2} & 0 \\ 0 & e^{i\phi_k/2} \end{bmatrix} \quad (3.28)$$

Defining a HR coating stack, the total transfer matrix from vaccum Q_0 to the N th coating layer is:

$$M = Q_N D_N \dots Q_k D_k \dots Q_1 D_1 Q_0 \quad (3.29)$$

The impact of a differential electric noise field (E) on M due to the electro-optic effect on the k th layer, we use the chain rule:

The coating to be studied consists 36 $\lambda/4$ thick layers of GaAs interspersed with 35 layers of $\lambda/4$ thick Al_{0.92}Ga_{0.08}As. GaAs forms the top and bottom layer to prevent oxygen absorption from the AlGaAs layer. The GaAs layers have an index of $n_{\text{GaAs}} = 3.480$ and a thickness of $\Delta d_{\text{GaAs}} = 76.43$ nm while the low index Al_{0.92}Ga_{0.08}As layers are $n_{\text{Al}_{0.92}\text{Ga}_{0.08}\text{As}} = 2.977$ with thickness $\Delta d_{\text{Al}_{0.92}\text{Ga}_{0.08}\text{As}} = 89.35$ nm. With the constructed matrices, we apply these parameters and compute a differential phase of:

3.0.6 Measured birefringence from HR GaAs/Al_{0.92}Ga_{0.08}As mirrors

There seems to be different accounts of a measured birefringence from HR GaAs / Al_{0.92}Ga_{0.08}As (Satoshi, CTN, Aidan)

Is the measured birefringence static? (Layer bonding method might introduce something?)
Does it change from different mounting methods? (Photoelastic) (order of magnitude estimate)

Measurement precision of the coating birefringence? Cavity length, Polarization drifts, etc.
The measured birefringence is estimated to be caused by an intrinsic strain between the epitaxial layers of GaAs/Al_{0.92}Ga_{0.08}As. [7]

Marty's document about Birefringence in Crystalline mirror coatings V.8

3.1 Projected DARM coupling

To estimate how much DARM coupling can occur, we use a measured field spectra acquired from installed electric field meters located within LIGO Hanford Observatory EX and EY vacuum chambers. Taking the upper and the lower EFM measurements in $.3 \text{ [V/m}/\sqrt{\text{Hz}}]$ @ 60 Hz and $4 \times 10^{-3} \text{ [V/m}/\sqrt{\text{Hz}}]$ @ 4kHz [14]. I don't think these values are calibrated. According to Martynov et al. 2016, the fluctuations in the electric field is $\sim 10^{-5} \text{ [(V/m)}/\sqrt{\text{Hz}}]$.

This along with computed estimate above allows us to create an upper limit for what this noise might be assuming incoherent fields between the end stations and a flat frequency response within LIGO's bandwidth.

FIGURE: GWINC noise against calibrated electro-optic noise estimate.

3.2 Short, in-air, Pound-Drever-Hall locked, Fabry-Perot cavity experiment

To attempt to acquire a calibrated estimate of the Electro-optic effect, we propose and use a single, in-air cavity, Pound-Drever-Hall servo to maintain resonance with a 1064nm carrier beam; while the GaAs/Al_{0.92}Ga_{0.08}As coated cavity end mirror installed in a custom longitudinal Pockels cell mirror mount. behind this work is the necessity to acquire a calibrated estimate of the pockels effect from a GaAs/Al_{0.92}Ga_{0.08}As mirror sample from Thorlabs' crystalline mirror coatings. As seen in the prior section, the size of the imparted phase noise for currently existing gravitational wave detector configurations is estimated to be small but notable. Investigation through measurement of said effect requires detection methods with sufficient sensitivity for the differential phase noise imparted by the effect. A Pound-Drever-Hall servo to maintain resonance of a 1064nm carrier field to a Fabry-Perot cavity, with the aforementioned crystalline coated cavity end mirror installed in a custom longitudinal pockels cell mirror mount was tried. Details and specifications of the detection schema are discussed along with relevant measurements and results.

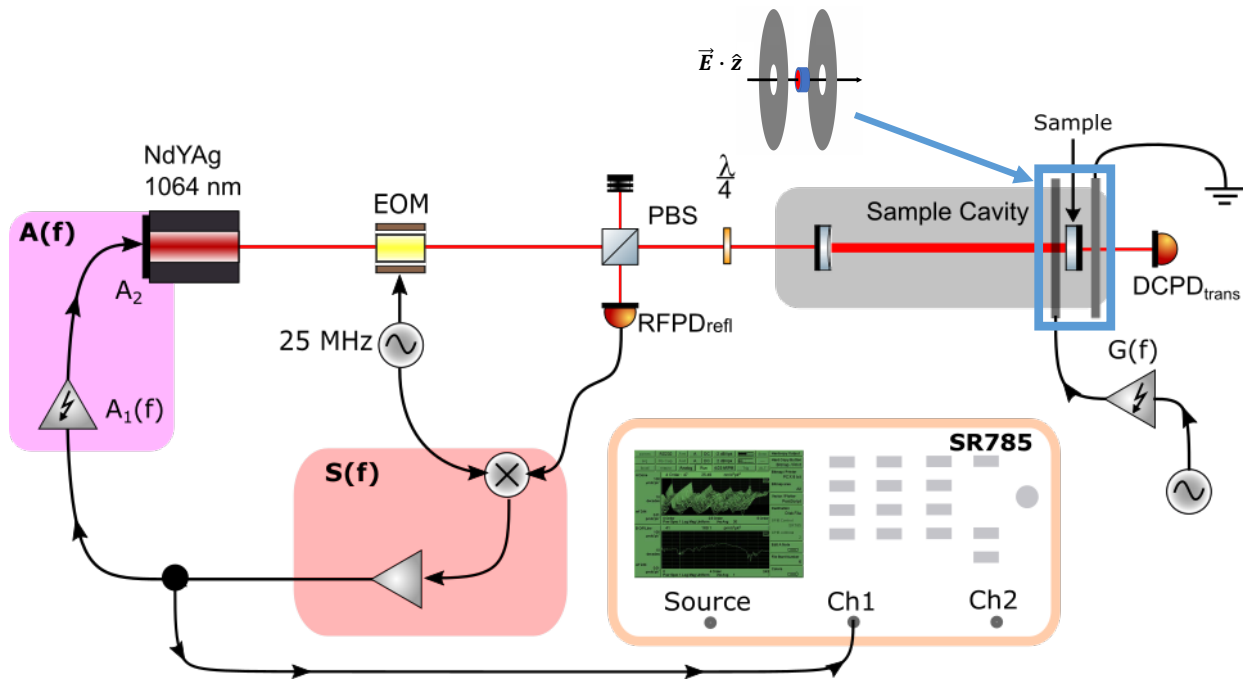


Figure 3.5: A simplified and modular schematic of the PDH servo used along with an electrostatic drive mount design comprised of a disk capacitor sandwiching the HR AlGaAs sample, a high voltage amplifier, and a signal / network analyzer.

Measurability of the electro-optic effect is contingent upon two initial design criteria: the sensitivity of the optical plant to be implemented in the PDH servo, and the maximum achievable electric field strength along the beam axis ($|E_z|_{\max}$).

3.2.1 PDH servo

The Pound-Drever-Hall technique, originally imagined for laser frequency stabilization to an ultra-stable length reference, allows the tracking of the linear phase response of an input carrier field through cavity resonance. The servo fully realizes the ability of an optical cavity to act as a length / frequency discriminator. The alternative cavity offset lock provides a linear response in intensity, which is adequate for some applications but with reduced sensitivity due to the required power reduction by operating off resonance.

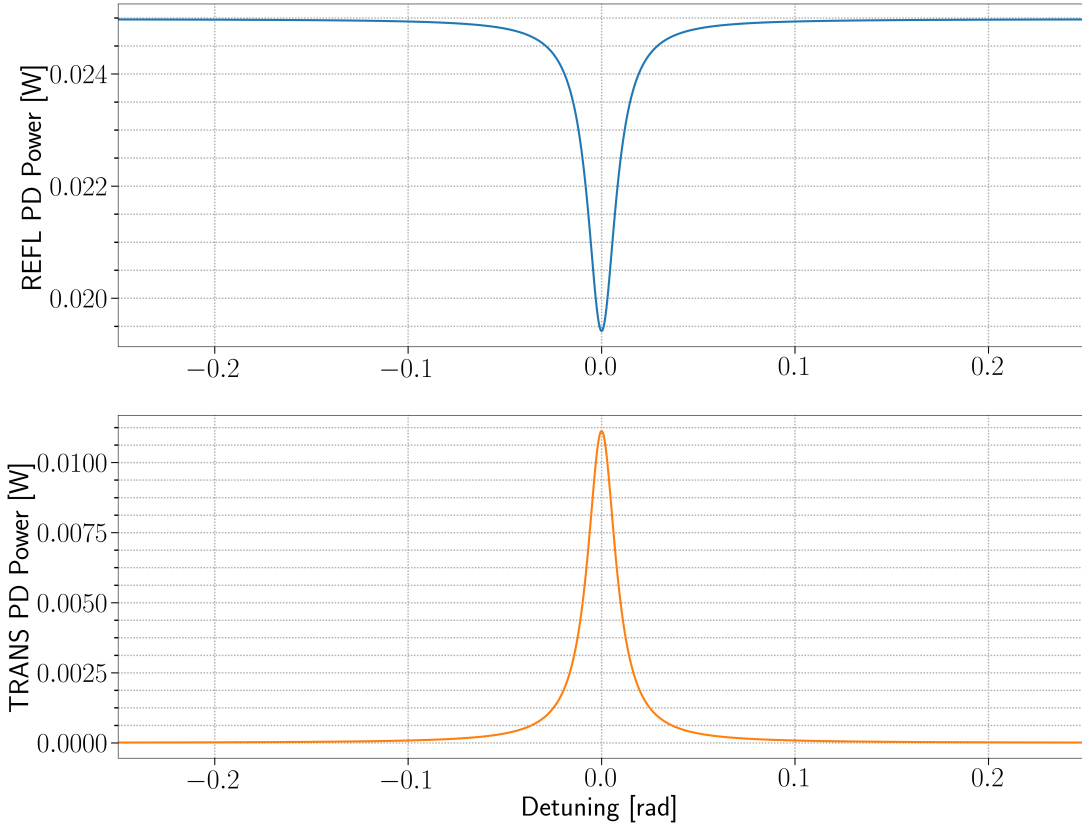


Figure 3.6: Reflected and transmitted power around resonance. Phase as dotted line?

The phase measurement is achieved through an optical heterodyne; the co-propagation of a separate (but phase-locked) optical field with a known frequency separation to the carrier reflected from the cavity input. To accomplish this, the PDH servo offers a way to avoid complicated phase-locked two laser configurations, by imposing a phase modulation on the carrier field via an electro-optic modulator (aka Pockels cell) mentioned in section 3.0.4. If the modulation depth given by 3.22 is set such that $\beta < 1$ then the input field may be approximated in terms of the first two Bessel functions J_0 , J_1 :

$$E_{\text{inp}} \approx E_0[J_0(\beta)e^{i\omega t} + J_1(\beta)e^{i(\omega+\Omega)t} - J_1(\beta)e^{i(\omega-\Omega)t}] \quad (3.30)$$

With a high enough modulation frequency the terms given above can be far enough from the carrier frequency, so that the phase modulation onto the carrier field is mathematically and physically equivalent to imposing separate optical fields (sidebands) which in most cases do not resonate in the optical cavity of interest. Setting a photodiode of area (A_{PD}) in reflection of the cavity with a coefficient of $r_{\text{cav}}(\omega, L)$, we measure the reflected power of the input field given by 3.30:

$$\begin{aligned} P_{\text{refl}} &\approx \frac{|E_{\text{refl}}|^2}{A_{\text{PD}}} \\ &\approx \frac{E_0^2}{A_{\text{PD}}} \left\{ J_0^2 |r_{\text{cav}}(\omega, L)|^2 + J_1^2(\beta) |r_{\text{cav}}(\omega + \Omega, L)|^2 - J_1^2(\beta) |r_{\text{cav}}(\omega - \Omega, L)|^2 + \right. \\ &\quad \left. J_0 J_1(\beta) [r_{\text{cav}}(\omega, L) r_{\text{cav}}^*(\omega + \Omega, L)] - J_0 J_1(\beta) [r_{\text{cav}}(\omega, L) r_{\text{cav}}^*(\omega - \Omega, L)] \right\} \end{aligned} \quad (3.31)$$

The two trailing terms in the above equation for P_{refl} generate a beat frequency term between the carrier and lower and upper sidebands. The magnitude and sign of these beat terms directly relate to the phase of the reflected carrier field and can be measured and transformed to the error signal seen in 3.7 using resonant electronics (tuned to a chosen sideband frequency) for amplification and a mixer for demodulation.

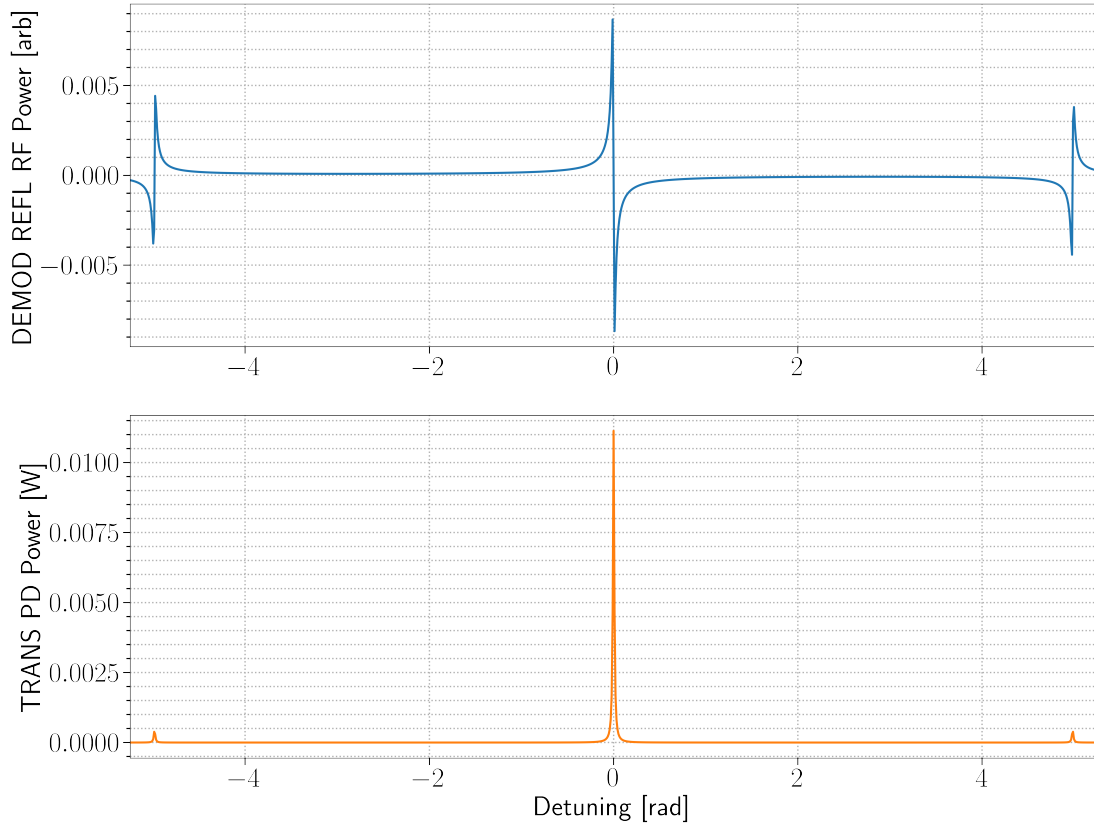


Figure 3.7: By imposing 25 MHz RF sidebands we have introduced a constant reflected reference field near carrier resonance which when beat with the carrier offers a linear response after demodulating the sideband power. With the introduction of high and low frequency sideband fields, their presence is also detected through the DCPDs and PDH error signal. Their separations from carrier resonance are equal in phase (length, and frequency).

With this linearity and sensitivity at cavity resonance, implementation into PID feedback is the next task as any small detuning of the cavity can be registered as a drift from the loop's zero point and fed back to an actuator with an estimated calibration gain factor. When implemented into a low-noise design, this servo can also be used for a high sensitivity lock-in measurement; and with well characterized instrumentation, calibration of the induced differential phase of the light within the stable reference cavity into differential length (or frequency).

3.2.2 Servo Parameters

The quantity we are attempting to measure is on the order of a length change of $\text{? m}/(\text{V/m})$, motivating a short cavity design as the relative differential length (phase) change scales with the sensitivity $\Delta f/f = \delta L/L$. Considerations of the lab mirror inventory and mode matching criteria lead us to two candidate plano-concave (ROC = 0.333m) HR IBS coated sample input couplers; one from CVI Melles-Griot and another from ATFilms. When paired with the plano-plano GaAs/Al_{0.92}Ga_{0.08}As mirror from the Crystalline Mirror Solutions (CMS) division of Thorlabs we create a 0.1665 m long cavity.

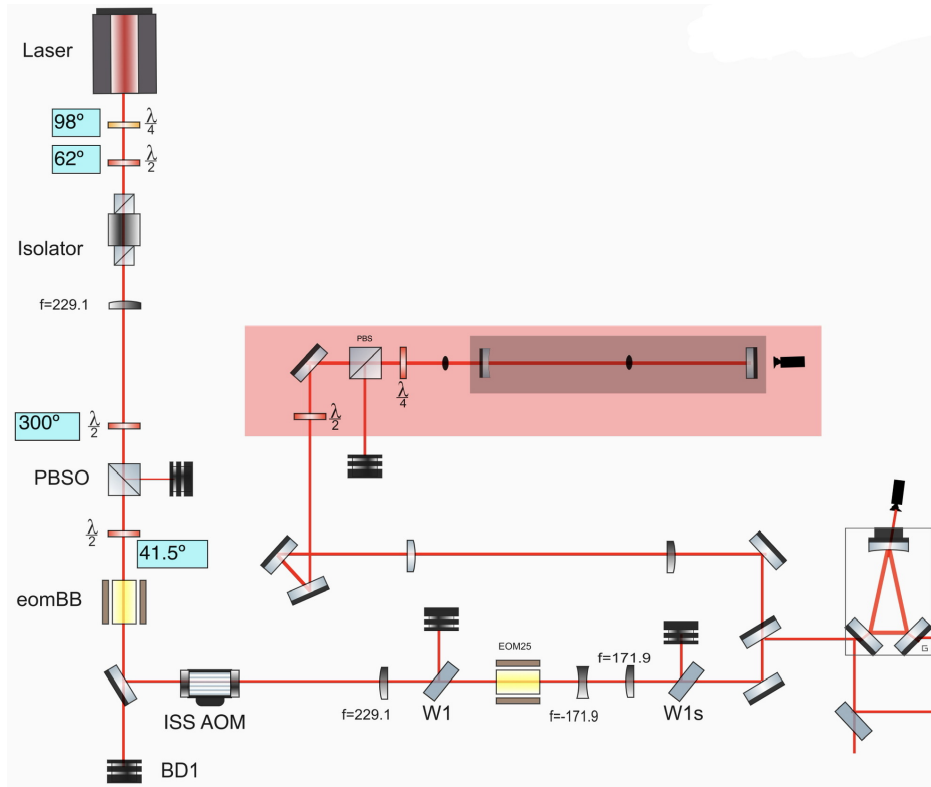


Figure 3.8: Final figure still pending Detailed optical schema of the experiment. Components highlighted in magenta indicate laser back-reflection protection and output power control. All optics highlighted in PURPLE indicate their function as alignment and mode matching for locking to a triangular ALIGO PMC **Multiple citations (DCC doc / Fabian's experiment / Erik's experiment)**. Optics highlighted in YELLOW indicate function for alignment and mode matching experimental cavity utilizing the HR GaAs/Al_{0.92}Ga_{0.08}As mirror. Beam profiling to the sample cavity is indicated. For the sake of the numerous mounting strategies tried, the longitudinal pockels cell mirror mount is kept general with the pictured mirror between two disk capacitors

FIGURE: Servo diagram caption: A simplified diagram of the servo used. The highlighted regions of the schematic are intended to provide a modular view; highlighting the components required for the PDH servo to operate.

The implemented servo design uses a light source from a Mephisto 2000 NE Nd:YAG (1064nm) laser with a 25 MHz phase modulation from a New Focus Model 4003 IR resonant phase modulator. As indicated in the figure above, the electronics chain can be decomposed into various filter components: $S(f)$, $A(f)$, and $A_{\text{thermal}}(f)$

Sensing S(f)

The sensing filter electronics are composed of a single element photodiode (from?) with a QE of ? and the response found in appendix ?. The signal is then mixed with a 25 MHz oscillator phased 180 degrees ? m of cable so the measured beat signal while sweeping through resonance generates the PDH error signal profile.

- 25 MHz RFPD
 - Transimpedance measurement (necessary? or should I just use the mixer out PDH to summarize PD/mixer response)
- Frequency Stabilization servo (modified MIT FSS (DCCD980536)) (LTspice model in appendix)

Actuation A(f)

- Mephisto 2220 PZT response (capacitance estimated from HVA drive measurement with and without connection to PZT)
- Channel 3 of SVR 350-3 BIP High Voltage Amplifier from Piezomechanik GmbH with Pomona box (elog 412)
- **Figure of frequency response of A(f)**

Low frequency servo (Thermal loop)

- Passed signal from FSS → integrators → Laser thermal actuator input

OLG(f)

Isn't quite $A(f) * S(f)$ as stated. Doesn't entirely account for the optical plant. How the measurement is taken (important to take between installations to account for the changes in the optical plant) (elog 831)

3.2.3 Longitudinal Pockels Cell mirror mount assembly

Maximizing the electric field ($|E_z|$) and within the coating while requiring a through beam to and through the HR coating lead us to a design very similar to that of a longitudinal pockels cell [1]. The assembly is comprised of two disk electrodes with a 3mm central aperture which is chosen to be at least 5 times larger than the beam size at the plate locations; to avoid significant beam clipping while maximizing field strength at the coating region of interest. There is also a required separation of at least 1/4" accounting for the thickness of the optical sample. Considering these constraints, modelling the system and computing the estimated field strength screened by the coating is the next step to the construction of the assembly.

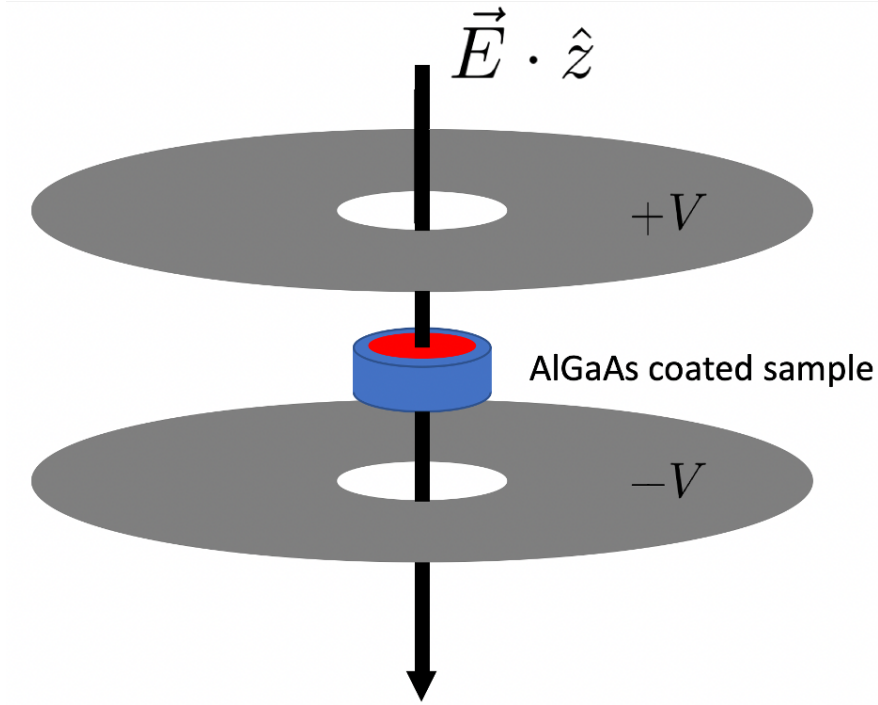


Figure 3.9: Concept image of the longitudinal Pockels cell assembly

Modelling

To find the Electric field screened by the coating we begin with Gauss' Law:

$$\nabla \cdot D = \rho_{\text{free}} \quad (3.32)$$

For our problem we assume no free charge, but the fused silica substrate with the AlGaAs coating presents dielectric material between the plates. Our initial boundary conditions are also expressed in terms of plate potentials so it is natural to first solve for the potential (V) for every point within our system. We can exploit the cylindrical symmetry with the optic and plate geometry in the r coordinate so we shall express the Laplacian accordingly:

$$(1 - \chi(z)) \left[\frac{1}{r} \frac{\partial}{\partial r} \left(r \frac{\partial}{\partial r} \right) + \frac{\partial^2}{\partial z^2} \right] V = 0 \quad (3.33)$$

Where $\chi(z)$ is the electric susceptibility.

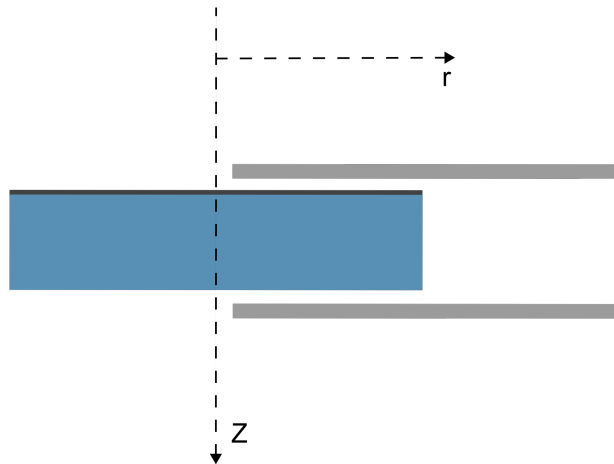


Figure 3.10: Use relevant cross sectional figure to establish coordinates for GaAs/Al_{0.92}Ga_{0.08}As, as well as the fused silica substrate so the computation is transparent. Cross sectional diagram indicating relevant axes and boundary conditions utilized in the numerical computation.

Numerical recipe in appendix

- Potential map computation in cylindrical
- Computing E_z from potential map
 - inside coating
 - outside coating

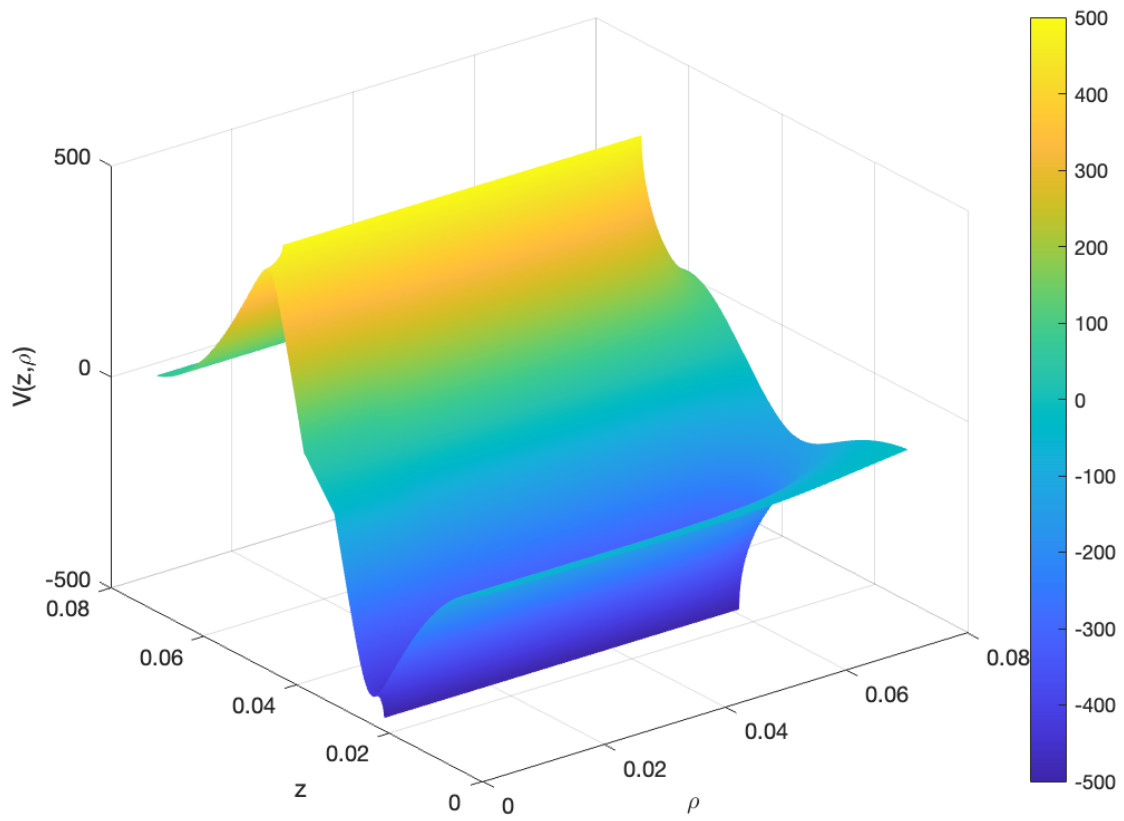


Figure 3.11: Poisson calculator output potential map ($V(z, r)$) in cylindrical coordinates)

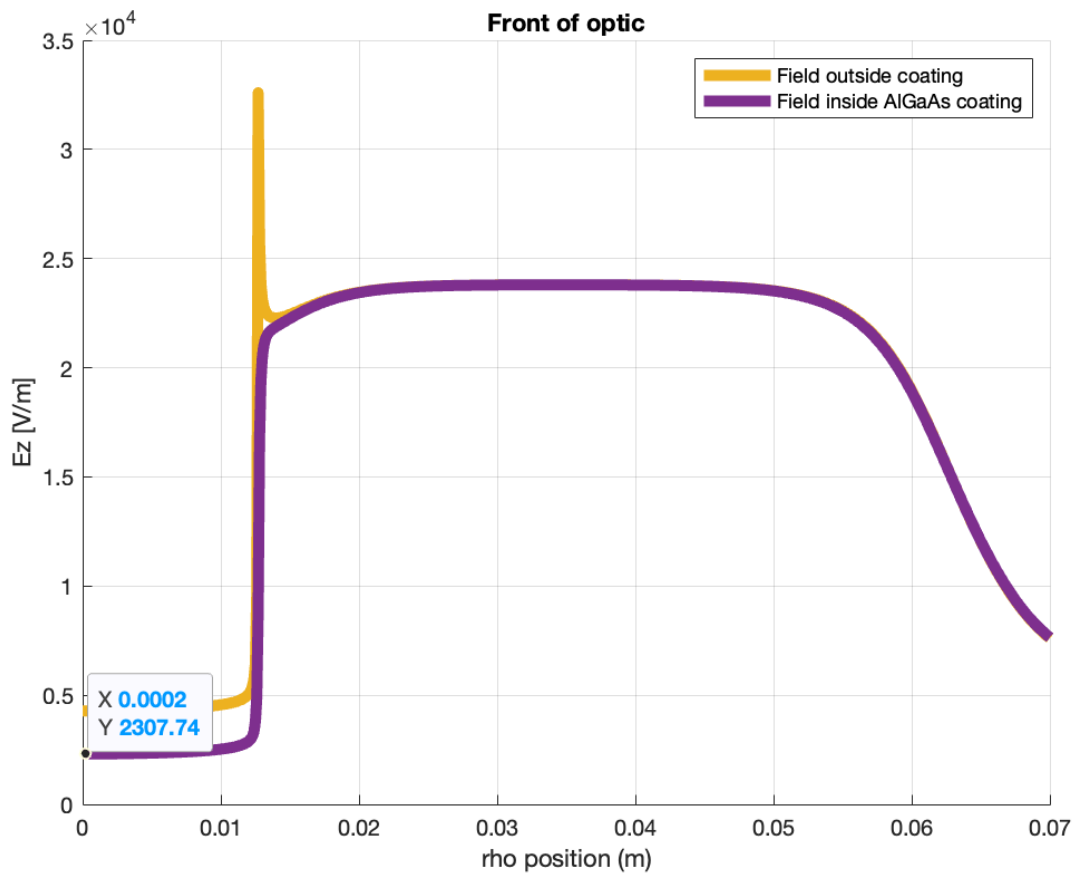


Figure 3.12: $|E_z|$ screened by the coating and immediately outside AlGaAs coating. Needs to be updated with more current voltage settings

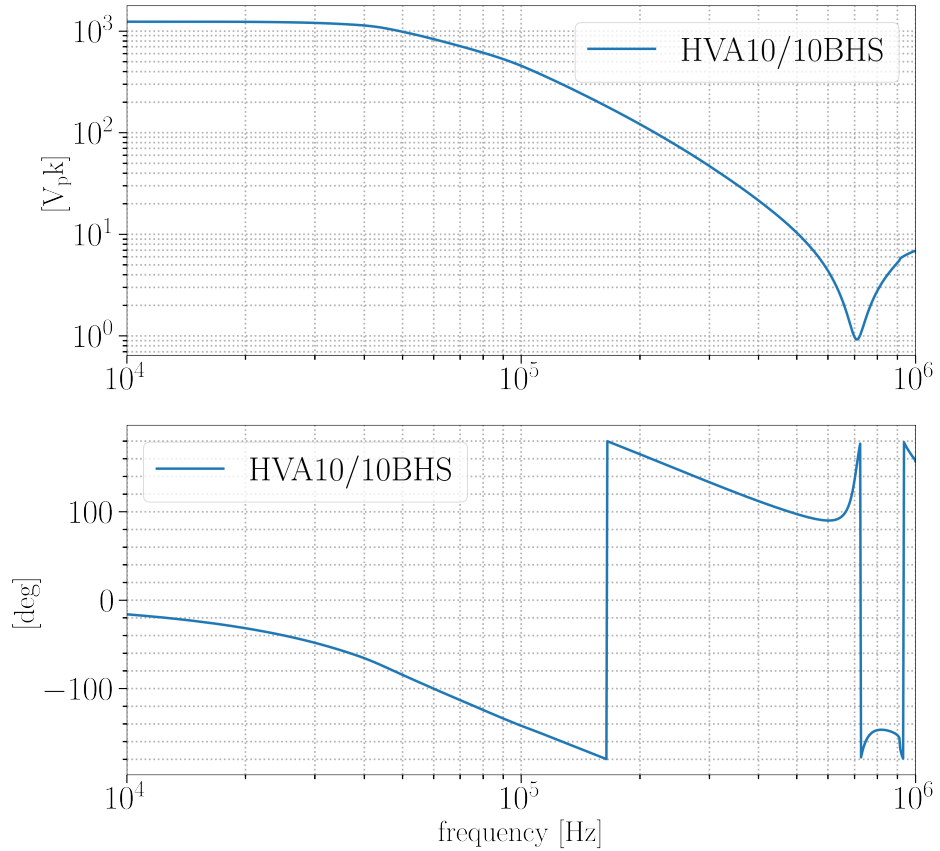


Figure 3.13: TREK 10/10B-HS HVA frequency dependent measurement. Using Poisson calculator to estimate field strength within coating. (Just HVA for now but will update. Also, assumes a flat response from coating within this studied region (is this a good assumption or could I do better? (dielectric frequency dependence))

3.3 Results

A major challenge encountered in the design choice made for this experiment is the differential length noise of the cavity when mounting the optics in accessible non-conductive materials. Most commercial optical mounts are conductors which proved to be a barrier when attempting to find a mounting solution while reducing non-normal field gradients within the coating volume of interest within the sample. For this reason, efforts were focused on developing a suitable mounting solution that would provide the best isolation from any uncontrolled field magnitudes while driving a field normally incident on the surface with enough strength and uniformity across the beam area to extract a measurement of the dif-

ferential length change from the Pockels effect. For reassurance, we installed a flat mirror with an amorphous coating to perform a null measurement reference; ruling out the Pockels effect and providing information for noise investigations.

3.3.1 Measurement Calibration

The error signal spectra probed at the FSS:

$$VFSSOUT_{rms}/\sqrt{Hz} \rightarrow m_{rms}/\sqrt{Hz} \quad (3.34)$$

With the the above servo electronics transfer functions, we calibrate the measurement into a differential length:

$$\Delta L = \text{source} * \alpha(f)A(f) * \frac{1 + OLG(f)}{OLG(f)} * \frac{L_{cav}}{f_{laser}} \quad (3.35)$$

3.3.2 Mounting Strategies

Assembly 0

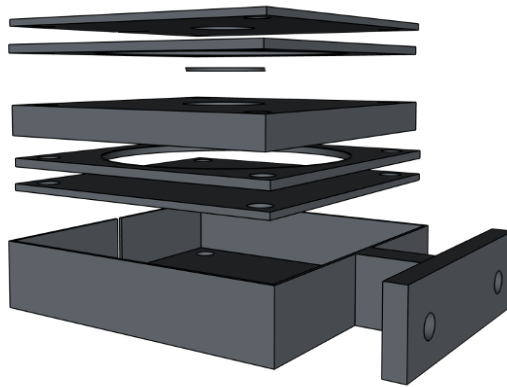


Figure 3.14: Assembly 0 was constructed to meet the criteria of providing a non-conductive housing for the electrode / sample assembly while maintaining a fixed length spacing using parts 3d printed with polylactic acid (PLA).

Difficulty locking from lack of angular control

Assembly 1

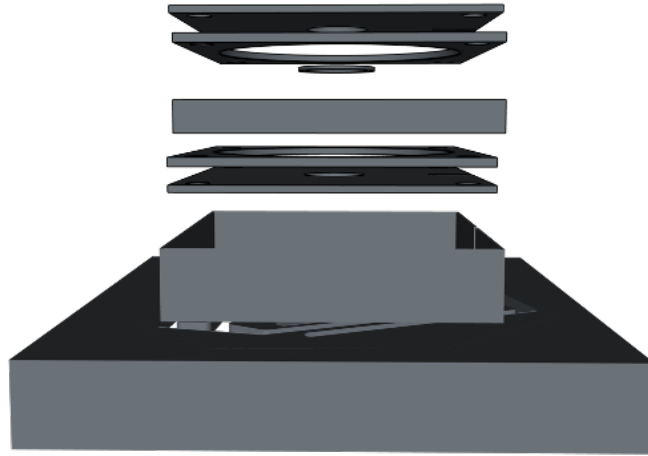


Figure 3.15: Assembly 1 was constructed to meet two criteria: the same solution of housing the sample and electrodes as Assembly 0, but also offer pitch / yaw control via an ortho-planar spring design (Brigham Young University).

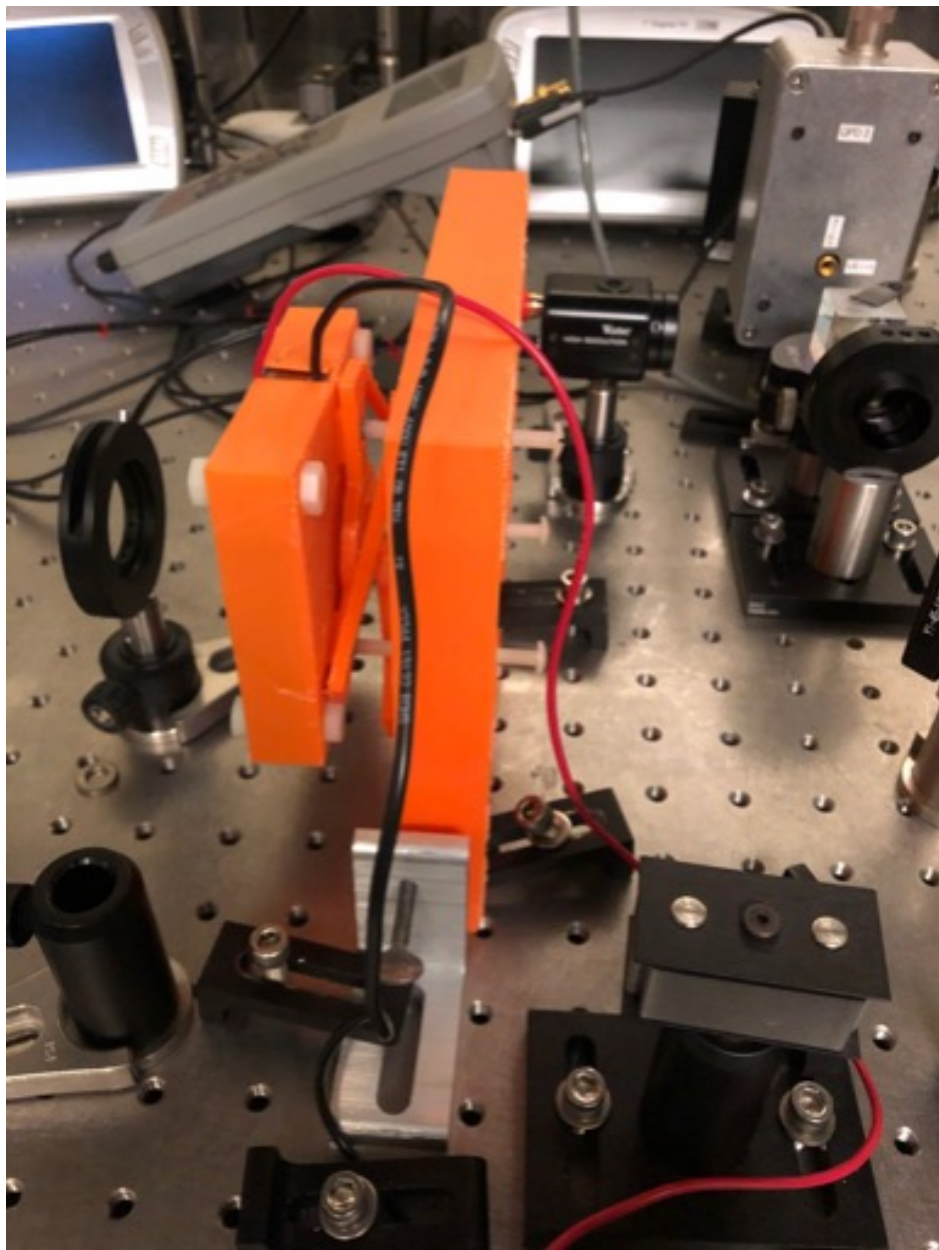


Figure 3.16: Assembly 1 pitch dithering design flaw

Looking through measurements for best noise measurements

Assembly 2

Different materials: PVC, PLA, PETG Copper electrodes

Assembly 3 (MACOR mount)

An optical mount made of MACOR a machinable ceramic with high a high Young's modulus (66.9 GPa), and a moderate Poisson ratio (.29) [15]. An optical mount for the sample made with MACOR, along with glass bearings .48 ± .01 cm \varnothing and a McMaster-Carr 8-32, 1/2" ceramic screw were used to clamp and suspend the optical sample. A 1.24" \varnothing hole was bored into the MACOR with a (depth?) depth so that there is a ? mm clearance between the front and back surface of the sample to the electrode plates. [Figure with the sample in-situ](#)



Figure 3.17: Placeholder for more updated MACOR assembly (this figure will end up in appendix to reference parts)

[Review notes and list all experiment configurations. Things modified from experiment to experiment: injection / measurement type \(single frequency and transfer functions \(with](#)

various ranges), mounts (Differing geometries, differing materials: PLA, PETG, MACOR), electrode sizes, separations, and assembly configurations

Looking through measurements for best noise measurements

3.3.3 Drive coupling

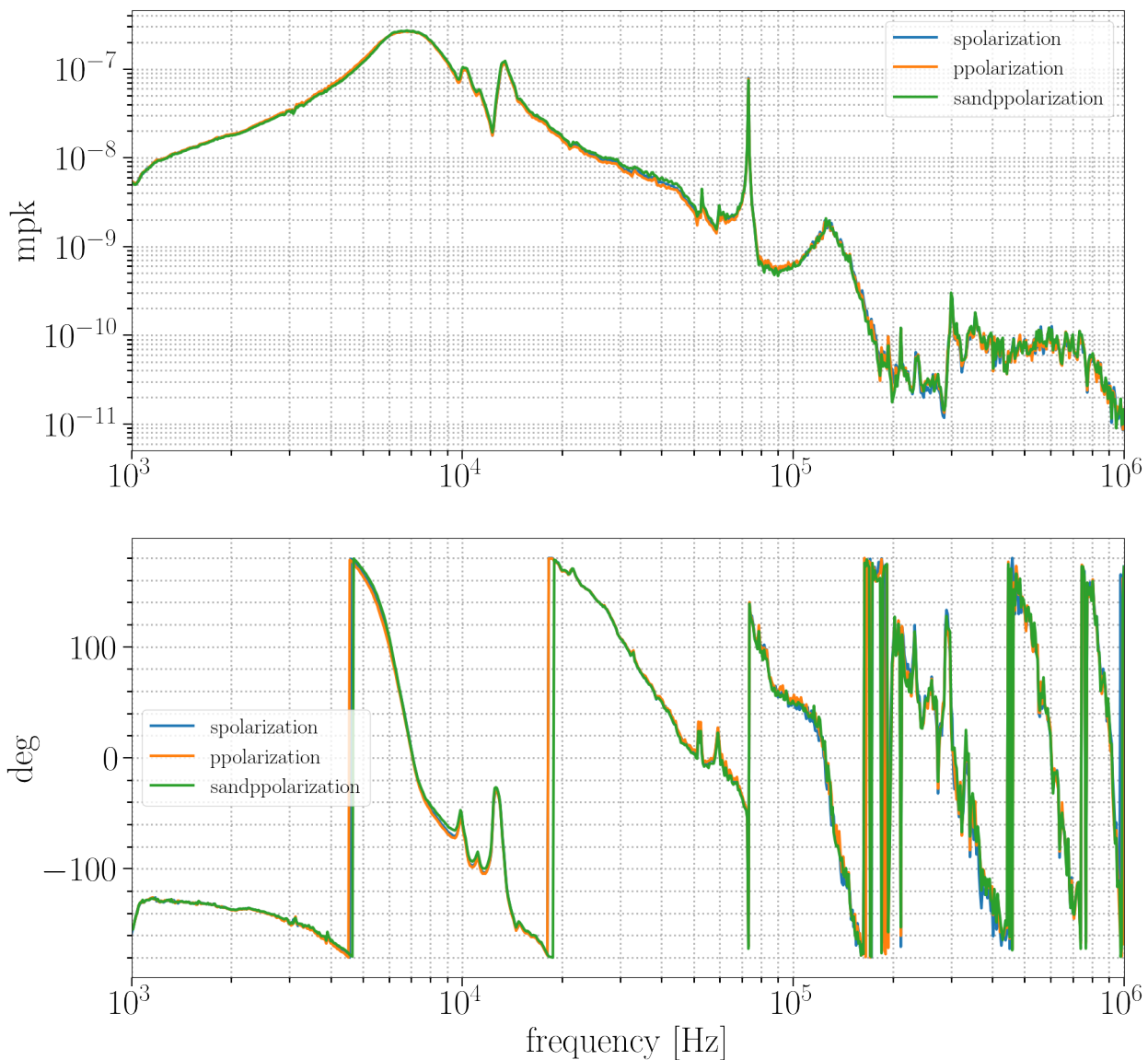


Figure 3.18: Figure that will include the all displacement noise floors, (pockels estimate)*(poisson calculator estimate)*(HVA drive frequency dependence), and the drive coupled measurement figure size needs to be increased

Opto-mechanical coupling

Sample and mount mechanical mode excitations. Seen with both AlGaAs and a HR coating from an AtFilm (IBS coating)

- **Vibration of plates (Leissa)** [16] Computing frequencies and order of magnitude
- Steve's COMSOL model results

Dual-polarization locked configuration

Chapter 4

Conclusion

The discovery of driven mechanical couplings within the longitudinal pockels cell mount are discussed and was shown to be a major limitation when using large (Mention range large) electric field injections indicated and have lead to an improved dual-polarization locked experimental design for improved sensitivity.

Satoshi results Though with limited sensitivity an upper limit with the experiment is established cite paper with Satoshi notes

Chapter 5

Appendix

5.1 The Equipartition theorem and the Fluctuation dissipation theorem

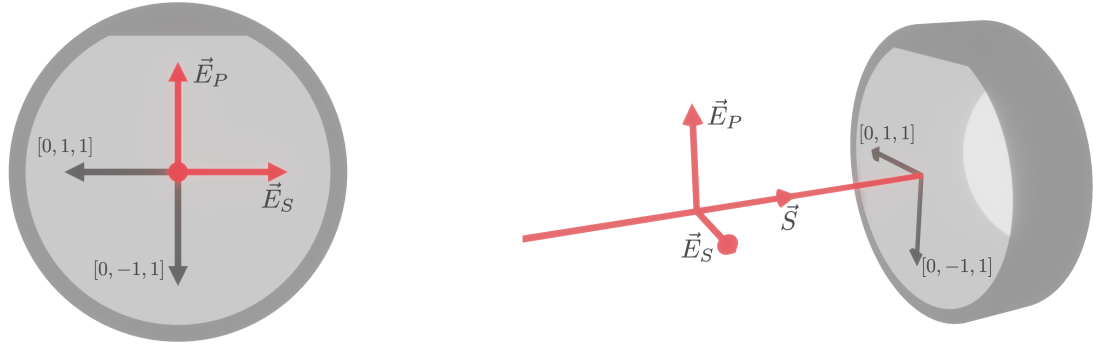


Figure 5.1: PENDING UPDATES Laser orientation with respect to the beam axis (isometric and normal views)

5.2 AlGaAs coating orientation to beam polarization

5.3 Mode matching data for Electro-optic sample cavity

5.3.1 Pre MMT beam scan

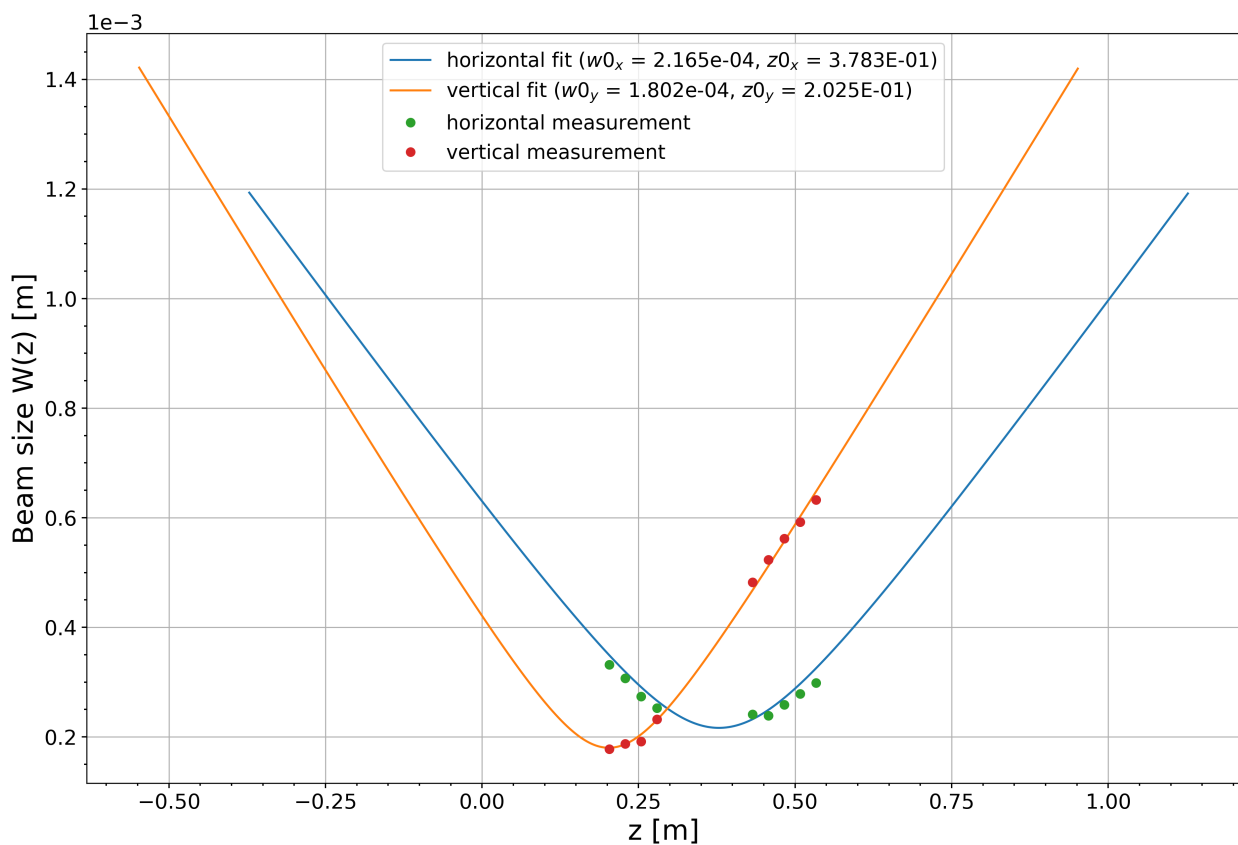


Figure 5.2: Beam scan taken from SM5 (Steering mirror 5)

5.3.2 “Just another mode matching tool” (JAMMT) solution

5.3.3 Post MMT beam scan

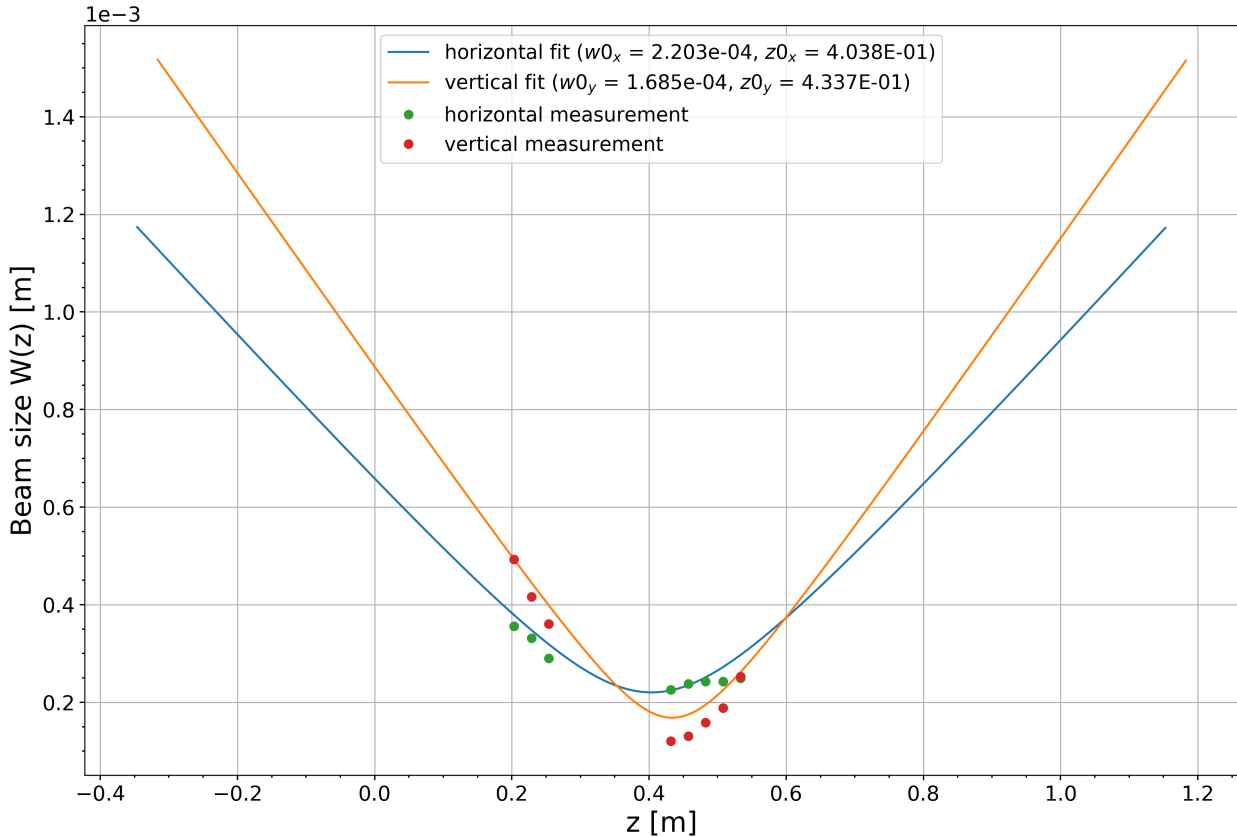


Figure 5.3: Beam scan taken from SM6. Sampling points before SM7 and after the first cavity iris.

5.3.4 Laser PZT sweep

5.4 Calibration

The frequency response measurement shown in (?) records the following transfer function in dB of the following:

$$\alpha(f) = \frac{\text{CH2}(f)}{\text{Source}} \quad (5.1)$$

Channel

We also know that the error signal spectra of the loop is probed by $CH2(f)$:

$$CH2(f) = \frac{S(f) * signal_V}{(1 - OLG(f))} \quad (5.2)$$

Where $signal_V$ is the uncalibrated voltage output from the mixer, $S(f)$ is the FSS transfer function, and $OLG(f)$ is the open loop gain of the PDH system.

And we know $OLG(f) = S(f) * A(f)$ so :

$$signal_m = CH2(f) * A(f) \frac{1 - OLG(f)}{OLG(f)} \frac{L_{cav}}{f_{laser}} \quad (5.3)$$

Where $A * (f)$ is the high voltage amplifier response with the Mephisto 2220 laser PZT response. L_{cav} is the sample cavity length, f_{laser} is the laser frequency. ($signal_m$) is the effective cavity length change from the Pockels effect.

Substitute (1) into (4):

$$signal_m = Source * \alpha(f) * A(f) \frac{1 - OLG(f)}{OLG(f)} \frac{L_{cav}}{f_{laser}} \quad (5.4)$$

Measured : Source, $\alpha(f)$, $OLG(f)$, $A(f)$ and L_{cav}

5.5 Laplace calculator / code

Snippets of explicit code with a block diagram for clarity

5.6 MACOR assembly

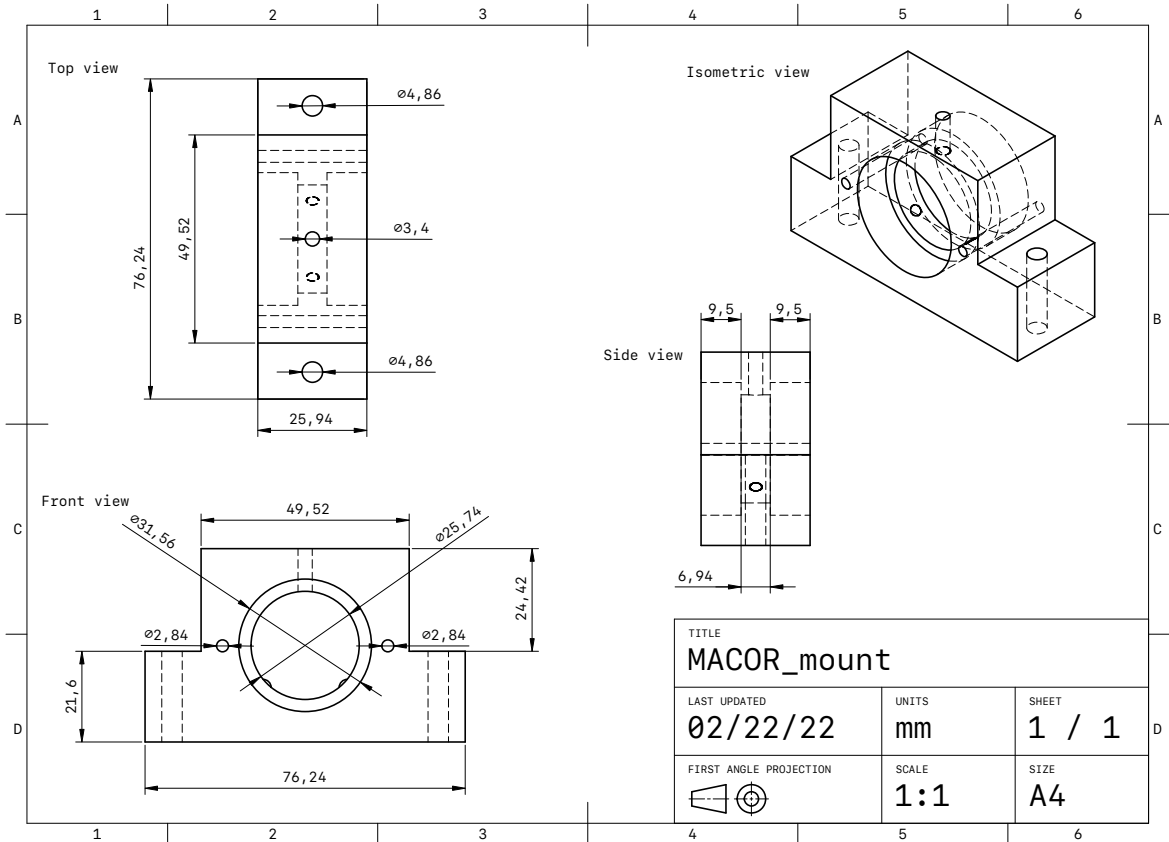


Figure 5.4: MACOR mount design constructed in Shapr3D

5.7 HVA

5.8 FSS

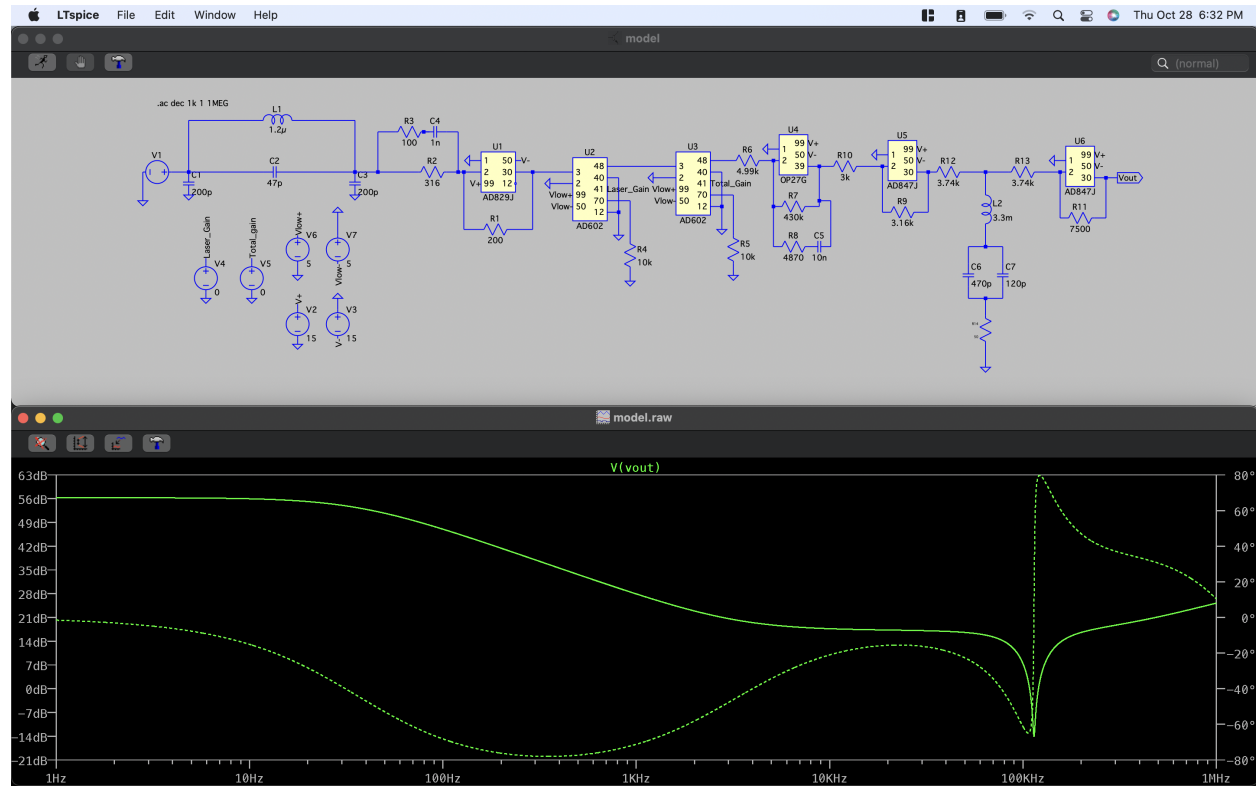


Figure 5.5: The FSS frequency response simulated in LTspice

References

- [1] R. B. F. H. M. . R. A. V.P.L.S., “Xxvii. a brief account of microscopical observations made in the months of june, july and august 1827, on the particles contained in the pollen of plants; and on the general existence of active molecules in organic and inorganic bodies,” *The Philosophical Magazine*, vol. 4, no. 21, pp. 161–173, 1828.
- [2] H. B. Callen and T. A. Welton, “Irreversibility and generalized noise,” *Phys. Rev.*, vol. 83, pp. 34–40, Jul 1951.
- [3] C. Zener, *Elasticity and Anelasticity of Metals*. University of Chicago Press, 1948.
- [4] Y. Levin, “Internal thermal noise in the ligo test masses: A direct approach,” *Physical Review D*, vol. 57, p. 659–663, Jan 1998.
- [5] T. Hong, H. Yang, E. K. Gustafson, R. X. Adhikari, and Y. Chen, “Brownian thermal noise in multilayer coated mirrors,” *Physical Review D*, vol. 87, Apr 2013.
- [6] G. M. Harry, H. Armandula, E. Black, D. R. M. Crooks, G. Cagnoli, J. Hough, P. Murray, S. Reid, S. Rowan, P. Sneddon, M. M. Fejer, R. Route, and S. D. Penn, “Thermal noise from optical coatings in gravitational wave detectors,” *Appl. Opt.*, vol. 45, pp. 1569–1574, Mar 2006.
- [7] G. D. Cole, W. Zhang, M. J. Martin, J. Ye, and M. Aspelmeyer, “Tenfold reduction of brownian noise in high-reflectivity optical coatings,” *Nature Photonics*, vol. 7, no. 8, pp. 644–650, 2013.

REFERENCES

- [8] T. Vo, *Adaptive Mode Matching in Advanced LIGO and beyond*. PhD thesis, Syracuse NY, 2019.
- [9] M. Abernathy, “Noise in crystalline coatings,” Tech. Rep. G1401060-v1, LIGO Scientific Collaboration, August 2014.
- [10] J. F. Nye, *Physical properties of crystals (Their representation by tensors and matrices)*. Oxford University Press, 1985.
- [11] A. Yariv, *Quantum Electronics (3rd. ed)*. John Wiley & Sons, 1989.
- [12] M. F. Edgard Bonilla, “Optical phase perturbations on the reflected wave of a dielectric mirror. application to the electro-optic effect in algaas coatings,” Tech. Rep. T1800528-v1, LIGO Scientific Collaboration, December 2018.
- [13] S. W. Ballmer, “Photothermal transfer function of dielectric mirrors for precision measurements,” *Physical Review D*, vol. 91, Jan 2015.
- [14] G. Mansell, “Electric field meter not coherent with darm (lho elog 56416).”
<https://alog.ligo-wa.caltech.edu/aLOG/index.php?callRep=56416>.
- [15] Corning, *MACOR (Machinable glass ceramic for industrial applications)*, 2012.
Available at <https://www.corning.com/media/worldwide/csm/documents/71759a443535431395eb34ebead091cb.pdf>.
- [16] A. W. Leissa, *Vibration of Plates*. National Aeronautics and Space Administration Special Publication (SP), 1969.